

踝蛋白

Extracellular rigidity sensing by talin isoform-specific mechanical linkages

Katharina Austen^{1,6}, Pia Ringer^{1,6}, Alexander Mehlich^{2,6}, Anna Chrostek-Grashoff¹, Carleen Kluger¹, Christoph Klingner¹, Benedikt Sabass³, Roy Zent⁴, Matthias Rief^{2,5} and Carsten Grashoff^{1,7}

The ability of cells to adhere and sense differences in tissue stiffness is crucial for organ development and function. The central mechanisms by which adherent cells detect extracellular matrix compliance, however, are still unknown. Using two single-molecule-calibrated biosensors that allow the analysis of a previously inaccessible but physiologically highly relevant force regime in cells, we demonstrate that the integrin activator talin establishes mechanical linkages following cell adhesion, which are indispensable for cells to probe tissue stiffness.
Talin linkages are exposed to a range of piconewton forces and bear, on average, 7–10 pN during cell adhesion depending on their association with F-actin and vinculin. Disruption of talin's mechanical engagement does not impair integrin activation and initial cell adhesion but prevents focal adhesion reinforcement and thus extracellular rigidity sensing. Intriguingly, talin mechanics are isoform specific so that expression of either talin-1 or talin-2 modulates extracellular rigidity sensing.

Tissue rigidity is an epigenetic factor that governs tissue patterning and organ development^{1–3}, while altered tissue mechanics is associated with numerous disease states including cardiovascular disorders, spinal cord injury or tumour formation^{4,5}. To distinguish differences in tissue stiffness, cells constantly probe the mechanical properties of their environment by anchoring and pulling on the surrounding extracellular matrix^{6–8} (ECM). This anchorage-dependent rigidity sensing is mediated by focal adhesions (FAs), subcellular structures in which ECM-binding integrin receptors are connected through adaptor proteins with the intracellular actin cytoskeleton^{9,10}. Although the important role of individual integrin subunits and distinct FA molecules such as focal adhesion kinase (FAK), paxillin or vinculin has been appreciated^{7,11,12}, the central mechanism that couples cell adhesion with mechanosensing remained unknown.

Among the implicated regulators of FA mechanosensing are talins, primarily known for their essential role during integrin activation¹³. Talins directly bind and thereby activate integrin receptors with an amino-terminal head domain and are thought to transduce mechanical information by simultaneously connecting to the actin cytoskeleton with their carboxy-terminal rod domain^{14–16}. Owing to the lack of suitable techniques to measure subcellular talin forces, however, quantitative evidence for mechanical tension across talin in cells was missing. We therefore embarked on the development of biosensors to examine the piconewton mechanics of talin linkages in living cells.

RESULTS

Single-molecule calibration of two genetically encoded tension sensors

We have previously generated a probe (called TSMod), in which an elastic peptide is flanked by two fluorophores allowing the measurement of molecular forces of 1–6 pN using Förster resonance energy transfer^{12,17–19} (FRET). Yet individual myosin motors can generate single piconewton forces²⁰ and forces across distinct integrin receptors were recently shown to be significantly higher^{21,22}. This suggests that the proteins that directly connect adhesion receptors with actomyosin networks such as talin may experience higher mechanical forces as well. We therefore engineered two tension sensors using the 35 amino acid-long villin headpiece peptide (HP35) as a force-sensitive element flanked by an YPet/mCherry pair of fluorophores (Fig. 1a). HP35 is an ultrafast-folding peptide that undergoes an equilibrium unfolding/folding transition in response to mechanical forces of about 7 pN, whereas a stable HP35 mutant (HP35st) undergoes this transition at about 10 pN (refs 23,24). To test whether HP35 unfolding/folding dynamics are affected by the presence of N- and C-terminally fused fluorophores, we performed

¹Max Planck Institute of Biochemistry, Group of Molecular Mechanotransduction, Martinsried D-82152, Germany. ²Technical University of Munich, Physics Department E22, Garching D-85748, Germany. ³Princeton University, Department of Mechanical & Aerospace Engineering, Princeton, New Jersey 08544, USA. ⁴Vanderbilt University, Division of Nephrology, Department of Medicine, Nashville, Tennessee 37232, USA. ⁵Munich Centre for Integrated Protein Science, Munich D-81377, Germany. ⁶These authors contributed equally to this work.

⁷Correspondence should be addressed to C.G. (e-mail: cgrasho@biochem.mpg.de)

Received 28 April 2015; accepted 8 October 2015; published online 2 November 2015; DOI: 10.1038/ncb3268

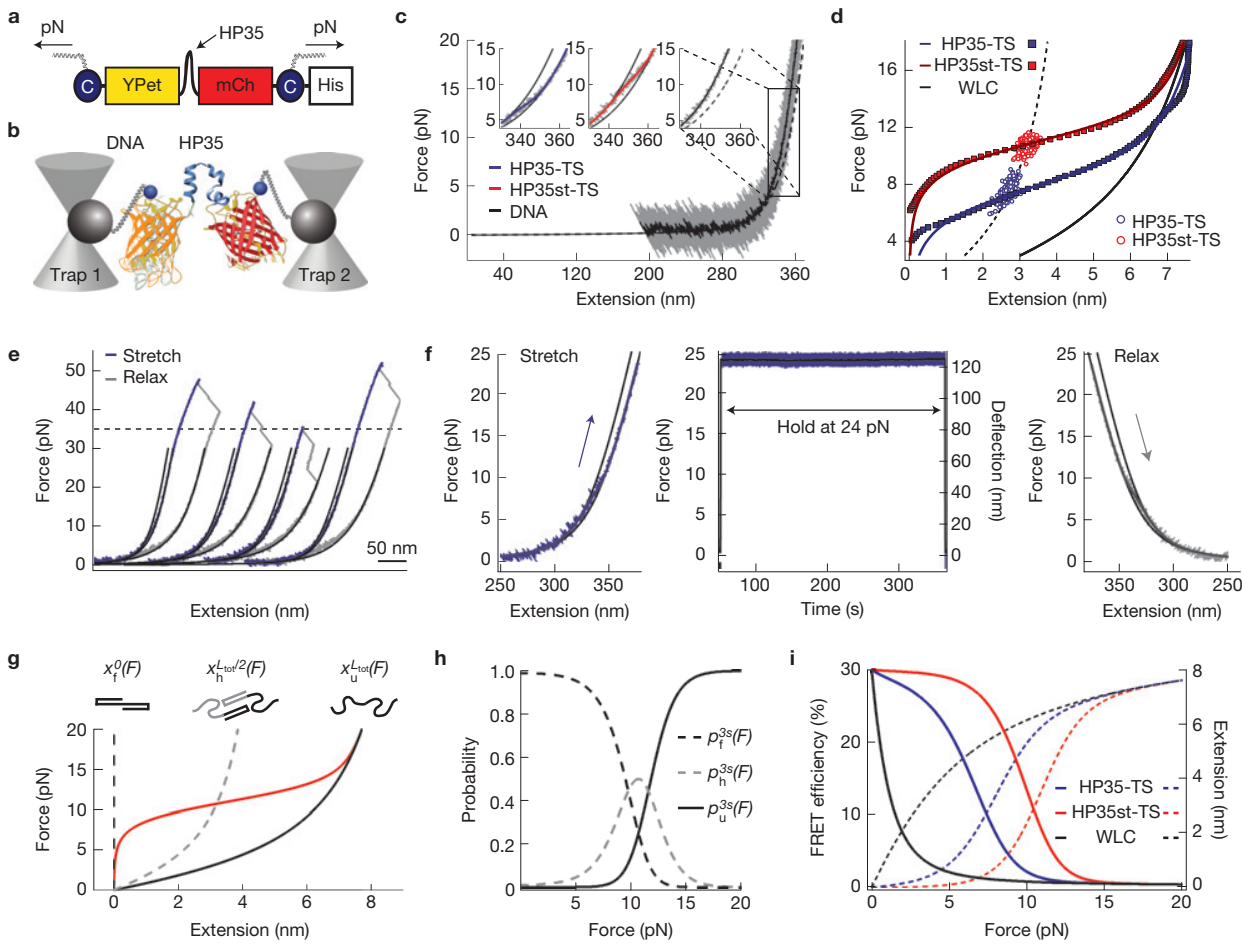


Figure 1 Biosensor calibration using single-molecule force spectroscopy. (a) HP35-TS comprises two fluorophores, YPet and mCherry (mCh), which are linked by the villin headpiece peptide (HP35). Mechanical force across this biosensor leads to HP35 unfolding, increase in fluorophore separation distance and reduced FRET. For single-molecule calibration, DNA handles were attached using cysteines (C), a His-tag was used for purification. (b) Schematic illustration of the dual-trap optical tweezer set-up used for calibration. (c) 200 kHz resolution force–extension trace (grey) fitted with an extensible worm-like chain model (black). Inset: zoom into representative force–extension traces of individual HP35(st)-TS molecules as compared to DNA; the fit to HP35-TS data is shown in blue, HP35st-TS in red and DNA in black. (d) Average force–extension traces of individual HP35-TS (blue) and HP35st-TS (red) molecules. Experimental data are shown as filled squares; solid lines are fits to the data; open circles represent transition midpoint forces (HP35-TS: $n=344$ single pulls pooled from

15 independent repeats, that is, different molecules; HP35st-TS: $n=338$ single pulls pooled from 10 independent repeats). (e) Force–extension traces of four representative HP35-TS molecules showing fluorophore unfolding at high (≥ 35 pN) forces following stretching (pulling velocity: 500 nm s^{-1}); traces were horizontally shifted for better representation. (f) After stretching to 24 pN, HP35-TS was exposed to high force for more than five min before relaxation; no indications of fluorophore unfolding were observed. (g) Average force–extension fit for HP35st-TS using a three-state model. The dashed black line represents the folded state, the grey dashed line the half-folded/half-unfolded state with contour length $L_{\text{tot}}/2$, and the black solid line the completely unfolded state with contour length L_{tot} ; the red line indicates the average protein extension (x_p). (h) Probability plot for the folded, half-folded/half-unfolded and unfolded state. (i) Modelled FRET-force (solid lines) and extension-force (dashed lines) correlations of HP35(st)-TS.

single-molecule calibrations using a custom-built optical tweezer set-up (Fig. 1b and Supplementary Note and Methods). As expected, the average equilibrium transition mid-forces were at 7.4 pN (HP35-TS) and 10.6 pN (HP35st-TS), and both sensors quickly recovered their original conformation when forces were released (Fig. 1c,d and Supplementary Fig. 1a–e). Importantly, unfolding of fluorophores was not observed below 35 pN (pulling velocity: 500 nm s^{-1} ; Fig. 1e) and also did not occur when constructs were subjected to a constant force of 24 pN for more than five minutes (Fig. 1f). The force–extension data of HP35-TS and HP35st-TS were well fitted by a three-state model assuming HP35(st) to be either in a folded, half-folded/half-unfolded or unfolded state (Fig. 1g and Supplementary Note and

Supplementary Fig. 1c,f–h). The resulting probabilities for HP35(st) to be in any of these conformations at a given force were used to calculate the biosensors’ force–FRET responses revealing highest sensitivity between 6–8 pN and 9–11 pN, respectively. (Fig. 1i). Thus, HP35-TS and HP35st-TS are efficiently folding, rapidly responding and reversibly switching tension sensors with response thresholds at about 7 pN and 10 pN.

Talin tension sensor evaluation

To examine talin forces in cells, we genetically inserted HP35-TS into the unstructured linker region connecting the head and rod domains of mouse talin-1 (Tln1TS; ref. 13). In parallel, we

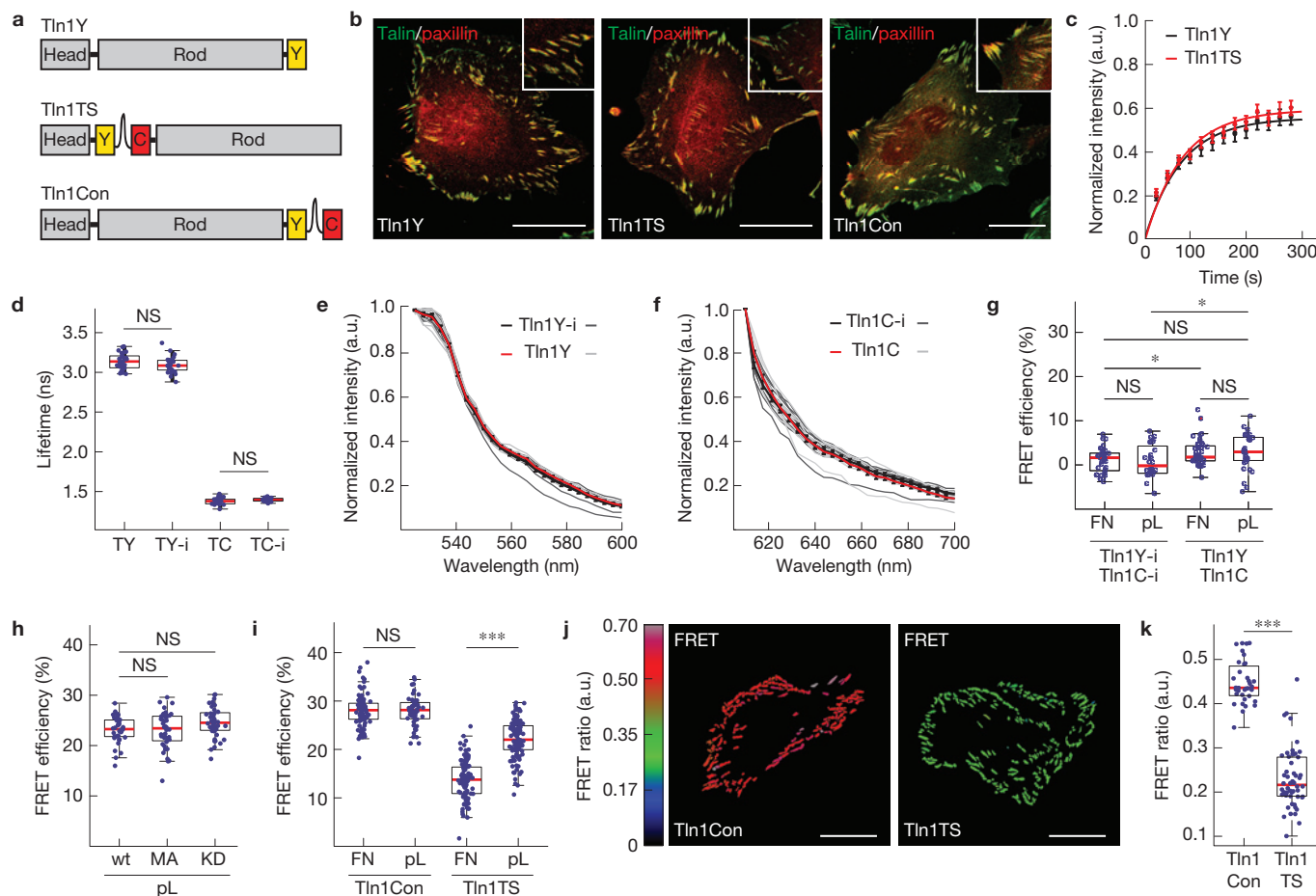


Figure 2 Generation and evaluation of the talin-1 tension sensor. **(a)** Schematic illustrations of C-terminally YPet-tagged talin-1 (Tln1Y), the talin-1-HP35 tension sensor (Tln1TS) and the talin-1 zero force control (Tln1Con). **(b)** Representative images from 4 independent experiments showing *Tln1^{-/-}/Tln2^{-/-}* cells expressing Tln1Y, Tln1TS or Tln1Con. Talin constructs are shown in green and paxillin in red; scale bars, 20 μm. **(c)** FRAP analyses demonstrating normal FA turnover rates of Tln1Y (black) and Tln1TS (red). Error bars indicate s.e.m.; $n=21$ and 24 cells respectively for Tln1Y and Tln1TS, pooled from 5 independent experiments. **(d)** Live-cell fluorescence lifetimes of internally and C-terminally tagged talin-1 constructs expressed in *Tln1^{-/-}/Tln2^{-/-}* cells ($n=29$, 28 , 30 , 23 cells respectively from left to right, 3 independent experiments). **(e)** Live-cell emission spectra of FA-localized Tln1Y-i (single measurements, dark grey lines; mean, black line) and Tln1Y (single measurements, light grey lines; mean, red line). Error bars indicate s.e.m.; $n=10$ and 10 cells, 3 independent experiments. **(f)** Live-cell emission spectra of FA-localized Tln1C-i (single measurements, dark grey lines; mean, black line) and Tln1C (single measurements, light grey lines; mean, red line). Error bars indicate s.e.m.; $n=10$ (Tln1C-i) and 10 (Tln1C) cells, 3 independent experiments. **(g)** Intermolecular FRET analysis in *Tln1^{-/-}/Tln2^{-/-}* cells co-expressing Tln1C-i/Tln1Y-i or Tln1C/Tln1Y on FN- or pL-coated glass coverslips ($n=35$, 28 , 44 , 36 cells respectively from left to right; 3 independent experiments). **(h)** No FRET efficiency differences in cells expressing Tln1TS (wt), Tln1TS-M319A (MA) and Tln1TS-K324D (KD) when seeded on pL-coated glass coverslips ($n=39$, 40 , 42 cells respectively from left to right; 3 independent experiments). **(i)** Live-cell FLIM analysis demonstrating decreased FRET efficiency in Tln1TS cells when seeded on FN-coated surfaces indicating tension across talin-1 ($n=35$, 56 , 102 , 115 cells respectively from left to right; 5 independent experiments). **(j)** Representative ratiometric FA FRET images of non-motile Tln1Con and Tln1TS cells confirming reduced FRET in Tln1TS cells; scale bars, 20 μm (3 independent experiments). **(k)** Mean ratiometric FA FRET in Tln1Con and Tln1TS cells ($n=32$ and 47 cells respectively for Tln1Con and Tln1TS; 3 independent experiments). **(d,g,h,i)**, Kolmogorov-Smirnov test, ***, $P<0.001$; *, $P<0.05$; not significant (NS), $P>0.05$. Box plots indicate the median (red line) as well as 25th and 75th percentiles; whiskers reach out to 2.7 standard deviations (σ). Statistic source data are available in Supplementary Table 1.

generated a C-terminally YPet-tagged control to test for talin function (Tln1Y), a C-terminally HP35-TS-tagged talin-1 to determine force-independent effects (Tln1Con; Fig. 2a), and intermolecular FRET controls in which the individual fluorophores were inserted into talin-1 (Tln1Y-i, Tln1C-i) or C-terminally attached (Tln1Y, Tln1C). Stable expression of these constructs in cells lacking talin-1 and talin-2 (*Tln1^{-/-}/Tln2^{-/-}*) revealed proper subcellular localization as well as rescue of the severe cell adhesion and FAK activation

defects of talin-deficient cells²⁵ (Fig. 2b and Supplementary Fig. 2a,b). Furthermore, fluorescence recovery after photobleaching (FRAP) experiments demonstrated normal FA turnover rates of Tln1TS as compared with Tln1Y (Fig. 2c), together indicating that insertion of HP35-TS does not impair talin function. Next, we confirmed that the fluorescence lifetimes and the emission spectra of donor and acceptor fluorophores were unaffected by the insertion into talin-1 (Fig. 2d-f), and we quantified effects of intermolecular FRET

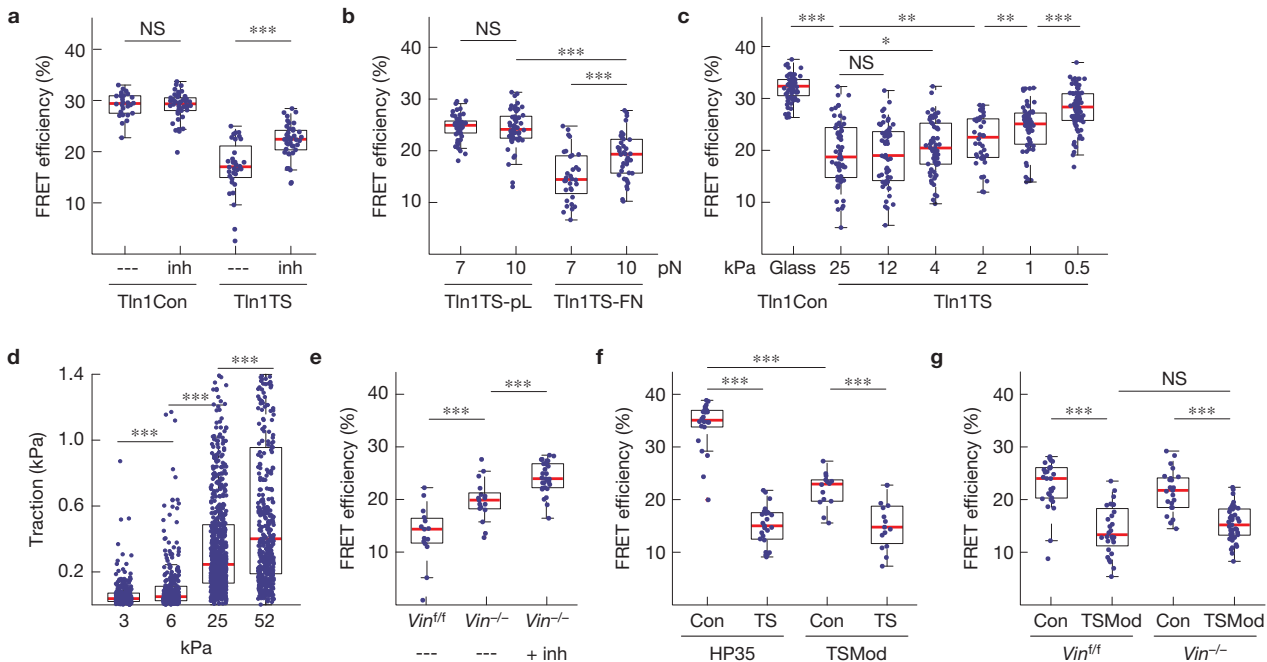


Figure 3 Talin-1 mediates a constitutive mechanical linkage in FAs that is modulated by F-actin and vinculin association. **(a)** Treatment of cells with $10\mu\text{M}$ Y-27632 (inh) induces an increase in average FRET efficiency specifically in Tln1TS cells ($n=26, 42, 32$ and 42 respectively from left to right; pooled from 3 independent experiments). **(b)** Comparing HP35-TS (7 pN) with HP35st-TS (10 pN)-based talin sensors in cells on FN- or pL-coated surfaces suggests that most talin-1 linkages experience force of more than 7 pN, some even more than 10 pN ($n=52, 53, 32$ and 40 cells respectively from left to right; 4 independent experiments). **(c)** FRET efficiencies in Tln1Con cells seeded on FN-coated glass coverslips ($n=68$) and in Tln1TS cells seeded on FN-coated 25kPa ($n=61$), 12kPa ($n=58$), 4kPa ($n=64$), 2kPa ($n=40$), 1kPa ($n=58$) and 0.5kPa ($n=81$) matrices; n represents the number of cells that were pooled from 5 independent experiments. **(d)** Rigidity-dependent traction force increase of Tln1Y cells seeded on FN-coated polyacrylamide gels with elastic moduli of 3.2kPa ($n=20$), 6.3kPa ($n=16$), 24.7kPa ($n=30$) and 52kPa ($n=15$); n represents the number of cells that were pooled

from 3 independent experiments. Single data points represent traction forces from displacement of every hundredth bead. **(e)** Depletion of vinculin leads to an increase in FRET whereas treatment of Tln1TS-expressing $Vin^{-/-}$ cells with $10\mu\text{M}$ Y-27632 further increases transfer rates indicating that loss of vinculin leads to a reduction but not entire loss of talin tension ($n=15, 17$ and 29 cells respectively from left to right, pooled from 7 independent experiments). **(f)** The HP35-based sensor monitors talin-1 tension more efficiently than a biosensor using TSMOD ($n=22, 25, 14$ and 15 cells respectively from left to right, 5 independent experiments). **(g)** TSMOD does not properly resolve vinculin-dependent differences in talin-1 tension ($n=29, 28, 25$ and 41 cells respectively from left to right, 3 independent experiments). **(a–c and e–g,** Kolmogorov–Smirnov test; **d,** Wilcoxon–Mann–Whitney test. $***, P<0.001$; $**, P<0.01$; $*, P<0.05$; not significant (NS), $P>0.05$.) Box plots indicate the median (red line) as well as 25th and 75th percentiles; whiskers reach out to 2.7 standard deviations (σ). Statistic source data are available in Supplementary Table 1.

(Fig. 2g), talin conformation (Fig. 2h), fluorescence intensity and temperature (Supplementary Fig. 2c,d) but found these confounding factors to be negligible in our experiments (see Methods for more detailed information). However, live-cell FRET analysis by time-correlated single-photon counting fluorescence lifetime microscopy or ratiometric imaging revealed an integrin-dependent reduction of energy transfer rates in Tln1TS cells indicating mechanical tension across talin-1 (Fig. 2i–k).

Talin-1 bears piconewton forces during cell adhesion

Next, we treated integrin-engaged Tln1TS and control cells with the Rock inhibitor Y-27632 to confirm that talin forces are actomyosin dependent. As expected, inhibitor treatment increased FRET efficiencies in Tln1TS cells but did not alter energy transfers in controls (Fig. 3a). Moreover, FRET efficiencies were specifically increased in integrin-engaged cells when the 9–11 pN-sensitive talin sensor (HP35st-TS) was used. Intriguingly, FRET was still lower than under control conditions indicating that a population of talin-1 molecules was subject to forces larger than 10 pN (Fig. 3b). To

test whether talin establishes mechanical linkages also in softer environments, we analysed cells on matrices characterized by elastic moduli of 0.5 – 25kPa . Tension across talin-1 was rather constant over a wide range of substrate rigidities and only gradually decreased on very soft substrates (Fig. 3c), although cells exhibited the expected rigidity-dependent reduction in traction forces as described before¹¹ (Fig. 3d). Thus, talin-1 mediates constitutive mechanical linkages, a significant subset of which experience forces of more than 7 pN and some even more than 10 pN.

High talin tension depends on association with mechanically engaged vinculin

Vinculin is an adaptor protein thought to regulate force transmission in FAs (refs 12,26,27). As the talin rod domain comprises 11 vinculin-binding sites¹³ (VBS), we examined talin tension by transiently expressing Tln1TS in vinculin-expressing ($Vin^{f/f}$) or vinculin-deficient ($Vin^{-/-}$) cells. These experiments suggested that talin-1 tension was decreased in the absence of vinculin, whereas tension was restored by stable re-expression of full-length vinculin (V-wt) but not by a

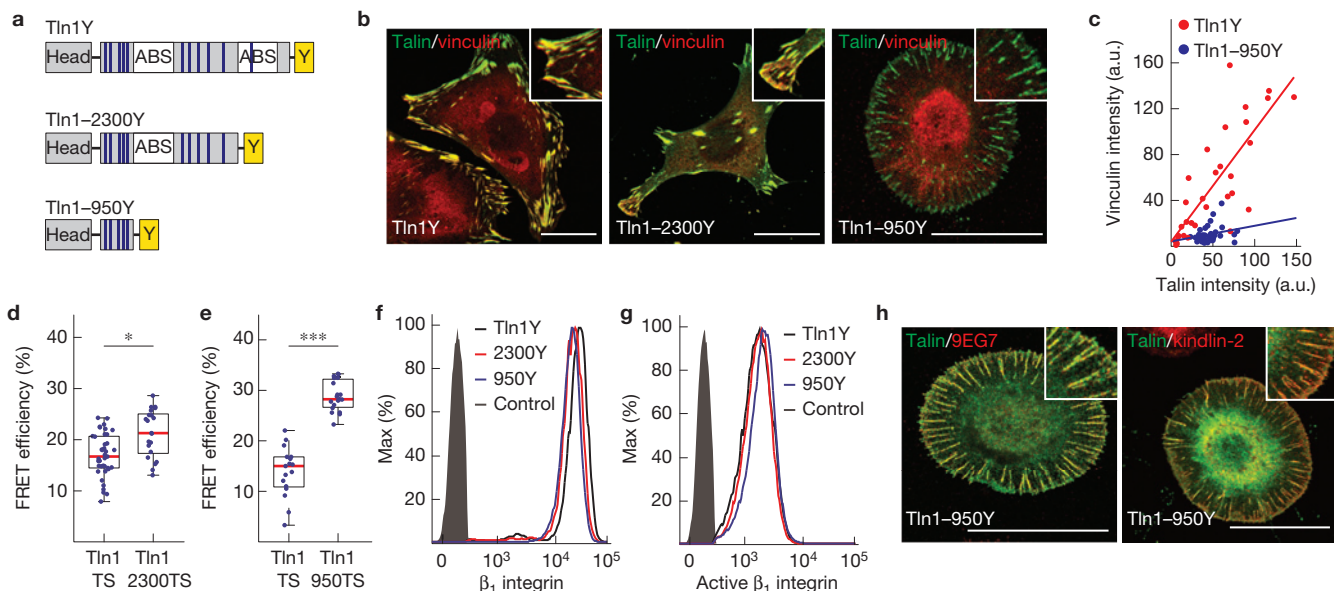


Figure 4 The talin-rod cytoskeletal engagement is essential for vinculin recruitment and talin tension but indispensable for integrin activation. (a) Schematic illustration of Tln1Y, Tln1-2300Y and Tln1-950Y constructs; blue lines indicate VBS, white rectangles ABS, yellow rectangles the C-terminal YPet-tag. (b) Representative images from 3 independent experiments showing *Tln1^{-/-}/Tln2^{-/-}* cells stably expressing Tln1Y, Tln1-2300Y and Tln1-950Y cells (green) stained with vinculin (red); scale bars, 20 μ m. (c) Talin-1/vinculin FA co-localization analysis demonstrating the lack of vinculin recruitment to talin-positive adhesion sites in Tln1-950Y cells ($n=32$ (Tln1Y) and 33 (Tln1-950Y) FAs, pooled from 3 independent experiments). Pearson correlation coefficient (talin versus vinculin intensity): Tln1Y = 0.8060, Tln1-950Y = 0.2424. (d) Moderate reduction in talin-1 tension following deletion of the dimerization domain and C-terminal ABS (Tln1-2300) ($n=39$ (Tln1TS) and 21 (Tln1-2300TS)

vinculin truncation mutant (V-mut) unable to transduce mechanical forces^{12,27,28} (Supplementary Fig. 2e). To confirm these results, we generated *Vin^{f/f}* and *Vin^{-/-}* cells stably expressing Tln1TS and again observed higher FRET efficiencies in vinculin-deficient cells that could be further increased by Y-27632 treatment indicating that forces across talin-1 were reduced but not entirely lost in the absence of vinculin (Fig. 3e). To investigate this in more detail, we generated a talin tension sensor using a YPet/mCherry version of our previously published 1–6 pN-sensitive probe¹² (TSMOD) and first analysed it in *Tln1^{-/-}/Tln2^{-/-}* cells. Consistent with our Tln1TS measurements, this construct also indicated tension across talin-1, even though FRET efficiency differences were smaller owing to the rather narrow dynamic range of TSMOD (Fig. 3f). In contrast to the HP35 probes, however, TSMOD-based sensors indicated very similar FRET values in *Vin^{f/f}* and *Vin^{-/-}* cells demonstrating that talin-1 is still subject to low forces of 1–6 pN in the absence of vinculin (Fig. 3g). Together, these results provide direct evidence that mechanical tension across talin-1 is determined by its association with F-actin and vinculin. While talin's F-actin engagement is sufficient to establish mechanically resilient linkages that bear low piconewton forces, vinculin binding seems to promote higher tension states. The results also underline the significance of the HP35 sensors that detect higher piconewton forces that cannot be resolved by TSMOD.

cells, 4 independent experiments). (e) Loss of talin-1 tension in Tln1-950 cells ($n=17$ (Tln1TS) and 19 (Tln1-950TS), 4 independent experiments). (f,g) Representative FACS histograms of 4 independent experiments showing cells expressing Tln1Y (black), Tln1-2300Y (red) and Tln1-950Y (blue) labelled for β_1 integrin (f) or active β_1 integrin (9EG7) (g); the negative control is shown in grey. Tln1-950Y cells exhibit normal integrin expression and activation. (h) Representative images from 3 independent experiments showing *Tln1^{-/-}/Tln2^{-/-}* cells reconstituted with Tln1-950Y (green) and labelled for active β_1 integrin or kindlin-2 (red). The recruitment of kindlin-2 in Tln1-950Y cells is consistent with normal integrin activation and cell adhesion; scale bars, 20 μ m. (d,e, Kolmogorov-Smirnov test. ***, $P<0.001$; *, $P<0.05$.) Box plots indicate the median (red line) as well as 25th and 75th percentiles; whiskers reach out to 2.7 standard deviations (σ). Statistical source data are available in Supplementary Table 1.

The mechanical engagement of the talin rod domain is dispensable for integrin activation but critical for vinculin recruitment to domains R1–R3

To elucidate whether vinculin recruitment to talin-1 depends on talin tension as proposed earlier^{15,29,30}, we generated mutants in which the C-terminal actin-binding sites (ABS) and VBS of talin-1 were deleted to varying degrees and stably expressed them in *Tln1^{-/-}/Tln2^{-/-}* cells (Fig. 4a). Removing talin's dimerization domain as well as the entire C-terminal ABS (Tln1-2300) resulted in less efficient cell spreading and impaired formation of peripheral actin bundles but only slightly reduced forces across talin-1 and hardly influenced vinculin's FA recruitment (Fig. 4b,d and Supplementary Fig. 3a). In contrast, deletion of the second ABS and six additional VBS (Tln1-950) strongly impaired cell spreading and stress fibre formation (Fig. 4b). Tln1-950 cells exhibited normal surface levels of activated β_1 integrin and readily adhered to ECM substrates forming integrin-, talin- and kindlin-2-positive adhesion sites (Fig. 4b-h). However, talin tension and vinculin recruitment were abolished even though Tln1-950 still harboured five VBS in the talin rod domains R1–R3 and vinculin was present at normal levels in the cytoplasm (Fig. 4b,c,e and Supplementary Fig. 3b,c). Together, the data indicate that vinculin association with talin-1's N-terminal VBS requires preceding cytoskeletal engagement. This observation is consistent with a previously suspected positive

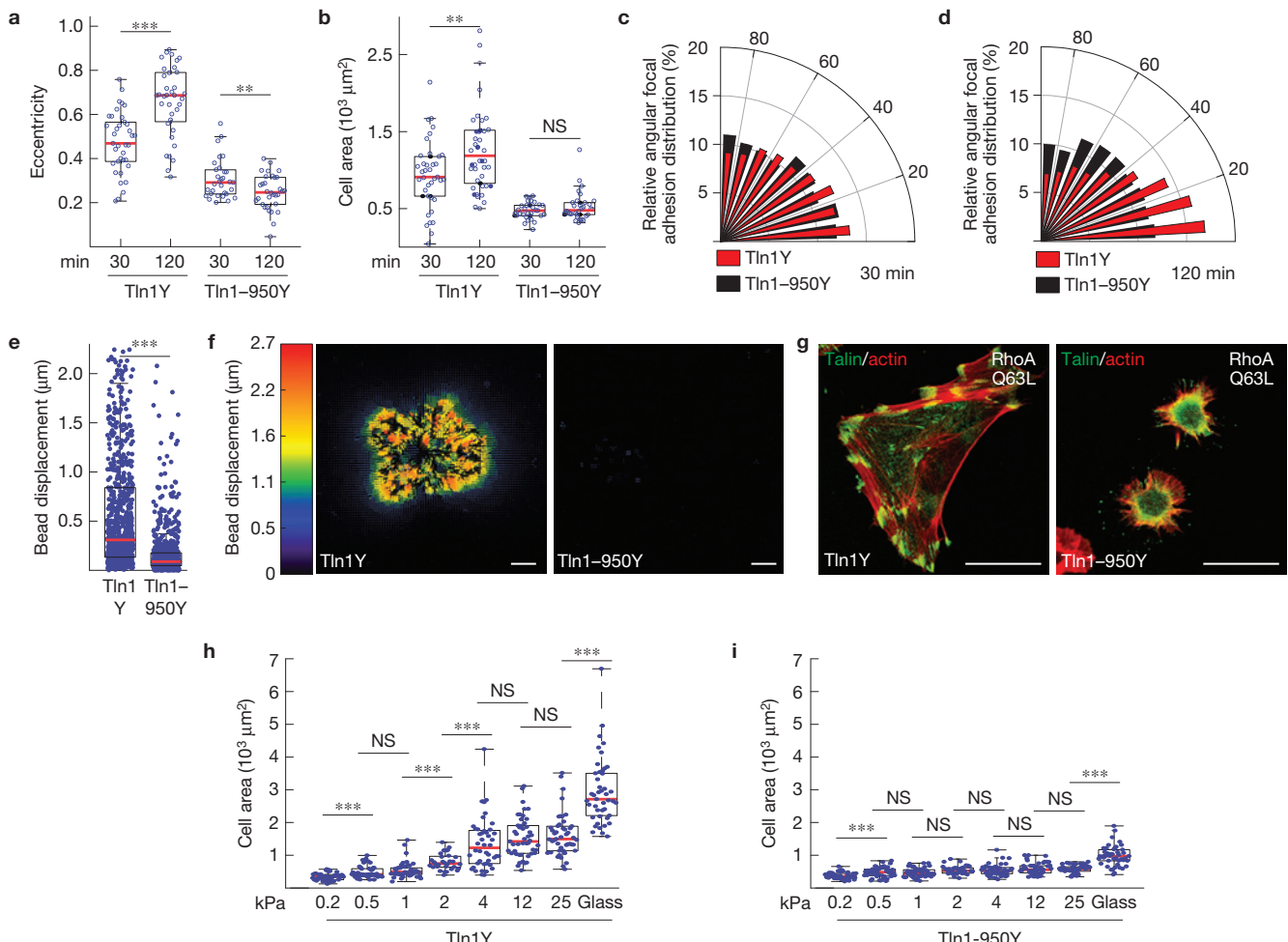


Figure 5 Cytoskeletal engagement of the talin-1 rod domain is indispensable for cell spreading, polarization, traction force generation and extracellular rigidity sensing. **(a,b)** Cellular eccentricity (**a**) and cell area (**b**) of Tln1Y and Tln1-950Y cells after 30 min or 120 min of spreading on FN-coated glass coverslips; Tln1-950Y cells are unable to polarize and spread (in **a** and **b** $n=37, 36, 31$ and 32 cells respectively from left to right, pooled from 3 independent experiments). **(c,d)** Relative angular FA distribution in Tln1Y cells (red) and Tln1-950Y cells (black) after 30 min (**c**) and 120 min (**d**) of spreading on FN-coated glass coverslips indicating lack of polarization in Tln1-950Y cells (in **c** and **d** $n=37$ (Tln1Y 30 min), 36 (Tln1-950Y 30 min), 31 (Tln1Y 120 min) and 32 (Tln1-950Y 120 min) cells, 3 independent experiments). **(e)** Bead displacements observed under Tln1Y ($n=21$) and Tln1-950Y ($n=22$) cells cultured on 2 kPa polyacrylamide gels; data were pooled from 4 independent experiments. Tln1-950Y cells are characterized by significantly lower traction forces indicated by very small bead displacements. **(f)** Representative displacement images (4 independent

experiments, corresponding quantification shown in **e**) of Tln1Y and Tln1-950Y cells indicating the virtual absence of traction forces in Tln1-950Y cells; scale bars, $10\mu\text{m}$. **(g)** Representative images from 3 independent experiments showing Tln1Y and Tln1-950Y cells (green) expressing active RhoAQ63L, stained for F-actin (red); Tln1-950Y cells fail to reinforce their FAs; scale bars, $20\mu\text{m}$. **(h,i)** Cell area of Tln1Y (**h**) and Tln1-950Y (**i**) cells after overnight culture on glass or FN-coated polyacrylamide gels with the indicated elastic moduli ranging from $0.2\text{--}25\text{ kPa}$; Tln1Y ($n=45, 45, 45, 32, 44, 47, 47$ and 45 cells respectively from left to right, 3 independent experiments), Tln1-950Y ($n=47, 49, 47, 32, 47, 46, 46$ and 45 cells respectively from left to right, 3 independent experiments). Note that Tln1-950Y cells fail to distinguish rigidity differences. **(a,b,h,i**, two-sided *t*-test; **e**, Wilcoxon-Mann-Whitney test. ***, $P < 0.001$; **, $P < 0.01$; *, $P < 0.05$; not significant (NS), $P > 0.05$). Box plots indicate the median (red line) as well as 25 th and 75 th percentiles; whiskers reach out to 2.7 standard deviations (σ). Statistic source data are available in Supplementary Table 1.

feedback regulation of FA strengthening, where F-actin-dependent vinculin engagement promotes talin tension leading to further vinculin recruitment at R1-R3 and cell adhesion reinforcement^{15,29-31}.

Talin linkages are essential for extracellular rigidity sensing

Throughout the experiments, we noticed that cell spreading and polarization, FA enlargement, and the generation of traction forces—all processes that require mechanical stabilization of FAs—were strongly impaired in Tln1-950 cells (Fig. 5a-f). Moreover, Tln1-950 cells failed to strengthen their FAs in response to increased

intracellular contractile forces after expression of active RhoA (RhoAQ63L) (Fig. 5g). We therefore tested whether extracellular rigidity sensing, which seems to require FA strengthening⁹, is affected in cells lacking mechanically engaged talin-1. Indeed, Tln1-950 cells seemed incapable of sensing and/or responding to different ECM rigidities whereas Tln1Y control cells reacted with the expected rigidity-dependent increase in cell area (Fig. 5h,i). Thus, the mechanical engagement of the talin rod domain with the actin cytoskeleton is indispensable for cell adhesion reinforcement and hence extracellular rigidity sensing.

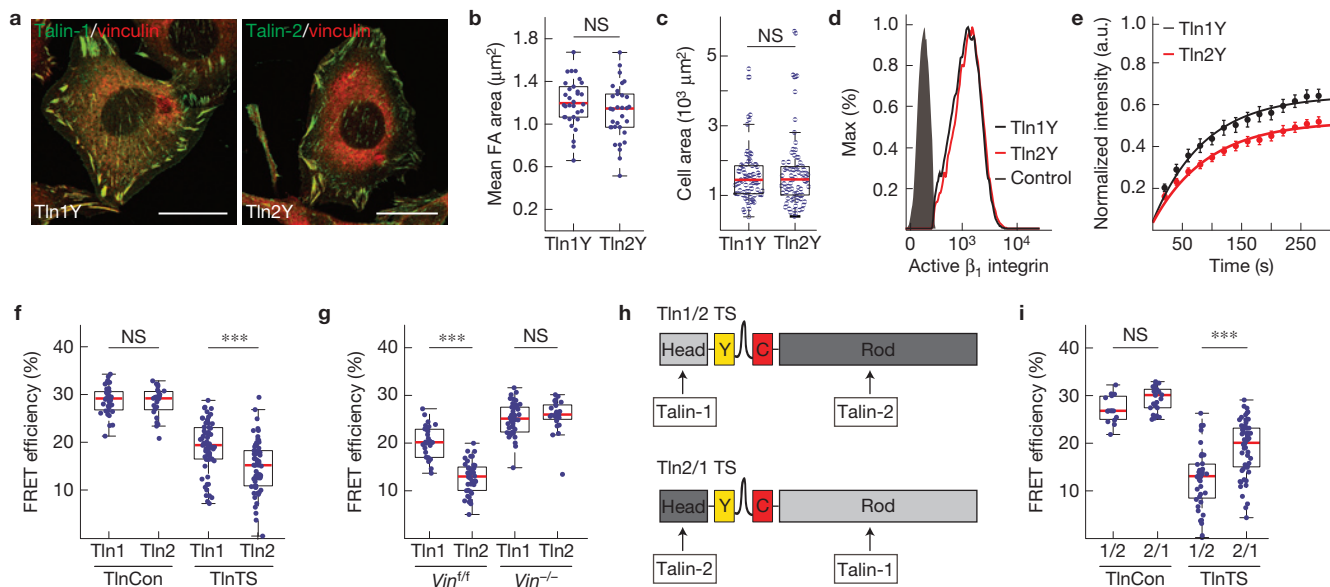


Figure 6 Talin-1 and talin-2 both rescue cell spreading and integrin activation but they transduce mechanical forces differently. **(a)** Representative images (3 independent experiments) of *Tln1^{-/-}/Tln2^{-/-}* cells reconstituted with Tln1Y or Tln2Y (green) and labelled for vinculin (red). Cell lines are indistinguishable when cultured on plastic or glass coverslips; scale bars, 20 μm. **(b,c)** Mean FA area ($n = 30$ (Tln1Y) and 34 (Tln2Y) cells; pooled from 4 independent experiments) **(b)** and mean cell area ($n = 77$ (Tln1Y) and 77 (Tln2Y) cells; 4 independent experiments) **(c)** determined from Tln1Y and Tln2Y cells seeded on FN-coated glass coverslips. **(d)** Representative FACS histogram of cells expressing Tln1Y (black) or Tln2Y (red) labelled for active β_1 integrin; the negative control is shown in grey (4 independent experiments). **(e)** Normalized fluorescence recovery rates of Tln1Y (black, $n = 18$ cells) and Tln2Y cells (red, $n = 17$ cells) as determined by live-cell FRAP experiments. Cells were pooled from 3 independent experiments; error bars indicate s.e.m. **(f)** FRET efficiencies in Tln1Con, Tln2Con, Tln1TS and Tln2TS cells ($n = 35$, 25, 63 and 63 cells respectively from left to right, 3 independent experiments) indicating increased tension across talin-2. **(g)** Isoform-specific tension differences are abolished in vinculin-deficient cells ($n = 28$, 41, 42 and 24 cells respectively from left to right; 3 independent experiments). **(h)** Schematic illustrations of chimaeric talin-1-head/talin-2-rod (Tln1/2-TS) and talin-2-head/talin-1-rod (Tln2/1-TS) tension sensor constructs. **(i)** FRET analysis of chimaeric talin constructs demonstrating that the isoform-specific tension increase is talin rod dependent ($n = 15$, 24, 43 and 58 cells respectively from left to right; 7 independent experiments). **(b,c)** two-sided *t*-test; **f,g,i**, Kolmogorov-Smirnov test. ***, $P < 0.001$; not significant (NS), $P > 0.05$. Box plots indicate the median (red line) as well as 25th and 75th percentiles; whiskers reach out to 2.7 standard deviations (σ). Statistic source data are available in Supplementary Table 1.

s.e.m. **(f)** FRET efficiencies in Tln1Con, Tln2Con, Tln1TS and Tln2TS cells ($n = 35$, 25, 63 and 63 cells respectively from left to right, 3 independent experiments) indicating increased tension across talin-2. **(g)** Isoform-specific tension differences are abolished in vinculin-deficient cells ($n = 28$, 41, 42 and 24 cells respectively from left to right; 3 independent experiments). **(h)** Schematic illustrations of chimaeric talin-1-head/talin-2-rod (Tln1/2-TS) and talin-2-head/talin-1-rod (Tln2/1-TS) tension sensor constructs. **(i)** FRET analysis of chimaeric talin constructs demonstrating that the isoform-specific tension increase is talin rod dependent ($n = 15$, 24, 43 and 58 cells respectively from left to right; 7 independent experiments). **(b,c)** two-sided *t*-test; **f,g,i**, Kolmogorov-Smirnov test. ***, $P < 0.001$; not significant (NS), $P > 0.05$. Box plots indicate the median (red line) as well as 25th and 75th percentiles; whiskers reach out to 2.7 standard deviations (σ). Statistic source data are available in Supplementary Table 1.

Integrin force transduction is talin isoform specific

Mammals express two very similar talin isoforms, the ubiquitous talin-1 and the more restrictively expressed talin-2. It is unclear why certain tissues require the expression of a second talin isoform, as both proteins efficiently activate integrins and connect to the cytoskeleton^{13,32}. We therefore wanted to test whether mechanical forces may be differentially transduced by talin-1 and talin-2 and generated a whole set of human talin-1 and talin-2 expression constructs to stably reconstitute *Tln1^{-/-}/Tln2^{-/-}* cells. Although individual expression of the talin isoforms rescued the cell spreading, integrin activation, and FAK phosphorylation phenotype of talin-deficient cells equally (Fig. 6a–d and Supplementary Fig. 4a–c), more talin-2 was immobilized in FAs (Fig. 6e and Supplementary Fig. 4d) and an increased number of talin-2 molecules were exposed to tension in integrin-engaged cells (Fig. 6f and Supplementary Fig. 4e–g). Elevated talin-2 tension levels were also observed in *Vin^{f/f}* but not in *Vin^{-/-}* cells, emphasizing the important role of the talin–vinculin interaction for generating high talin forces (Fig. 6g). To confirm that differences in isoform-specific talin tension were mediated exclusively by the talin rod domain, we engineered chimaeric talin constructs, in which the C-terminal domains of talin-1 and talin-2 were exchanged (Fig. 6h). Stable expression of these constructs rescued the cell adhesion and cell spreading defect of talin-deficient cells, and

FLIM experiments demonstrated that the tension increase was indeed entirely mediated by the rod domain of talin-2 (Fig. 6i). Next, we generated a talin-2 truncation mutant lacking all C-terminal ABS but retaining the five VBS residing in R1–R3 (Tln2–950) analogous to the talin-1 construct described above. Remarkably, Tln2–950 FAs were vinculin-positive, exposed to mechanical tension and able to induce, albeit not completely rescue, cell spreading (Fig. 7a–d). Together, these results show that the two human talin isoforms bear mechanical forces differently; they also suggest that the F-actin-dependent vinculin recruitment to talin’s N-terminal rod domain, specifically to domains R1–R3, is talin-1 specific.

Isoform-specific effects are mediated by the talin rod domains R1–R3

As our data indicated that initial vinculin recruitment to talin-2 is independent of preceding force generation through F-actin association, we tested whether FA strengthening and cell spreading on low-rigidity substrates, where actomyosin contractility is naturally reduced, is talin isoform dependent. Indeed, talin-2 cells spread more efficiently than talin-1 cells on 1–2 kPa matrices but behaved like talin-1-expressing cells on very soft (0.2–0.5 kPa) and more rigid (4–25 kPa) substrates (Fig. 7e). To test whether the observed isoform-specific effects are mediated by the talin rod domains R1–R3,

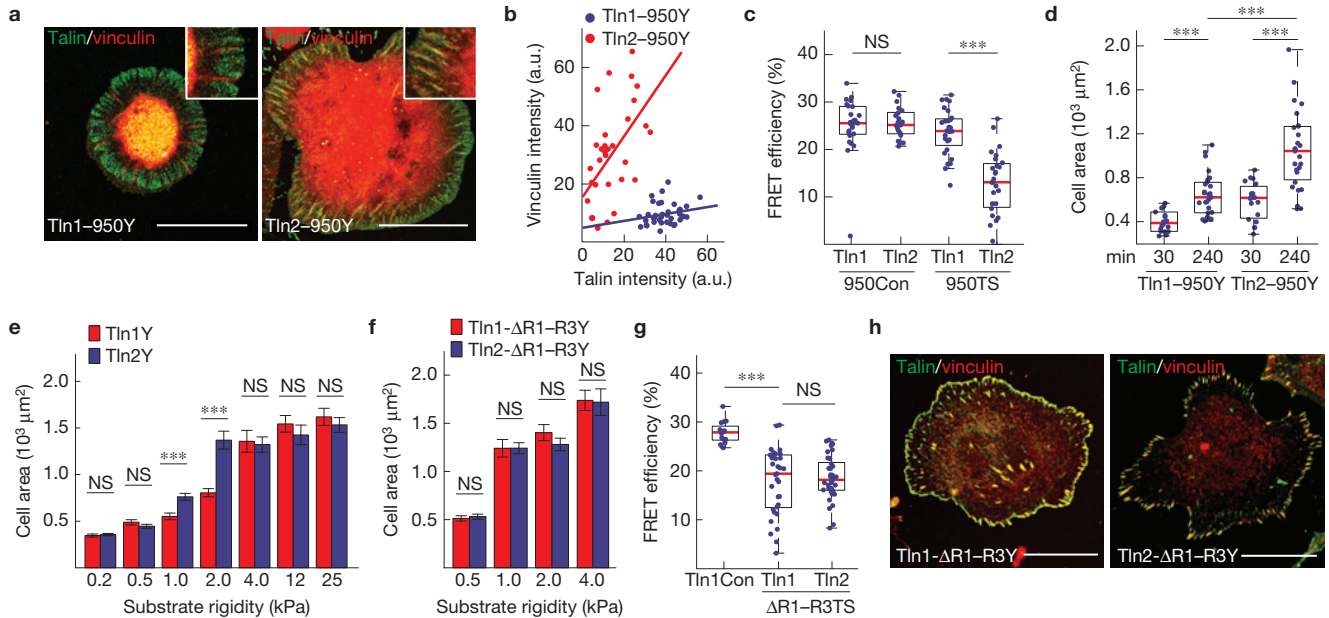


Figure 7 Talin isoform-specific differences are mediated by domains R1–R3. **(a)** Representative images from 3 independent experiments showing that vinculin (red) co-localizes with Tln2-950Y but not with Tln1-950Y adhesion sites; scale bars, 20 μm. **(b)** Quantification of talin/vinculin co-localization in adhesion sites of cells expressing Tln1-950Y ($n=32$ adhesions) and Tln2-950Y ($n=38$ adhesions); n values represent pooled adhesions from 3 independent experiments. Pearson correlation coefficient (talin versus vinculin intensity): Tln1-950Y = 0.2214, Tln2-950Y = 0.5323. **(c)** Deletion of C-terminal ABS abolishes tension across talin-1 but not across talin-2 ($n=24, 21, 28$ and 25 cells respectively from left to right; 5 independent experiments). **(d)** Cell area of Tln1-950Y and Tln2-950Y cells after 30 min and 240 min spreading on FN-coated glass coverslips ($n=18, 27, 19$ and 27 cells respectively from left to right; 3 independent experiments). **(e)** Cell area quantification of Tln1Y and Tln2Y cells seeded on FN-coated substrates of indicated stiffness; Tln2Y cells respond differently on 1 kPa and 2 kPa matrices ($n=47, 49, 45, 46, 45, 48, 32, 30, 44, 47, 48, 48, 46$ and 46 cells respectively from left to right; 3 independent experiments; data are means \pm s.e.m.). **(f)** No differences in cell spreading of Tln1-ΔR1R3Y ($n=50$ (0.5 kPa), 50 (1 kPa), 53 (2 kPa) and 47 (4 kPa) cells) and Tln2-ΔR1R3Y cells ($n=52$ (0.5 kPa), 47 (1 kPa), 47 (2 kPa) and 47 (4 kPa) cells). Cells were pooled from 3 independent experiments; data are means \pm s.e.m. **(g)** FRET analysis of talin-deficient cells expressing Tln1-ΔR1R3TS and Tln2-ΔR1R3TS constructs seeded on FN-coated glass coverslips ($n=16, 33$ and 37 cells respectively from left to right; 3 independent experiments). **(h)** Representative images from 3 independent experiments showing Tln1-ΔR1R3Y and Tln2-ΔR1R3Y cells on FN-coated glass coverslips stained for vinculin; the talin signal is labelled in green, the vinculin signal is shown in red; scale bars, 20 μm. **(c,g)**, Kolmogorov–Smirnov test; **d–f**, two-sided *t*-test. *** $P < 0.001$; not significant (NS), $P > 0.05$. Box plots indicate the median (red line) as well as 25th and 75th percentiles; whiskers reach out to 2.7 standard deviations (σ). Statistic source data are available in Supplementary Table 1.

we generated talin-1 and talin-2 expression constructs in which these domains were deleted (Tln1-ΔR1-R3). Indeed, *Tln1^{-/-}*/*Tln2^{-/-}* cells expressing talin-1 or talin-2 ΔR1-R3 deletion constructs did not exhibit differences in cell spreading on 1–2 kPa substrates and differences in talin tension were abolished (Fig. 7f,g). As vinculin was still efficiently recruited by the remaining VBS (Fig. 7h), we conclude that the observed talin isoform-specific effects are mediated by talin's N-terminal rod domains R1–R3.

DISCUSSION

The ability of cells to efficiently sense their mechanical environment is critical for many developmental, homeostatic and pathological processes^{1–6}. Yet the underlying molecular mechanisms have been difficult to elucidate because suitable methods to study force propagation across individual molecules in cells were missing. We therefore developed a biosensor that allows molecular force measurements at 1–6 pN and the technique has been widely used to determine forces across various proteins in living cells and even whole organisms^{12,17,18,33–37}. An obvious limitation of the method, however, has been its inability to resolve forces higher than 6 pN. In this work, we describe the generation, single-molecule calibration and application of two biosensors

that enable efficient measurements at 6–8 pN and 9–11 pN. The probes are characterized by sharp and very fast force responses, they are reversible, benefit from an improved dynamic range and do not unravel until forces of about 35 pN are reached (Fig. 1).

Application of these biosensors revealed that the integrin activator talin establishes mechanical linkages during cell adhesion that are indeed subject to forces larger than 7 pN; furthermore, a small but significant fraction of talin molecules experiences forces of more than 10 pN. On the other hand, talin tension dropped to relatively low levels in the absence of vinculin binding and disappeared on talin's disengagement from the actin cytoskeleton (Figs 2 and 3). Thus, talin bears a range of forces depending on the degree of its mechanical engagement and it should be worthwhile investigating how talin tension correlates with FA dynamics for instance during cell migration. Interestingly, the formation of force-bearing talin linkages occurred over a wide range of substrate rigidities and seemed inherently linked to the formation of enlarged FAs. Consistent with this observation, cells expressing a truncated talin mutant lacking all C-terminal F-actin-binding sites (Tln1-950) were unable to form large FAs; they failed to generate significant cellular traction forces and did not sense extracellular rigidity differences even

though integrin activation was unaffected (Figs 4 and 5). Thus, in addition to its crucial role as an integrin activator, talin is an indispensable mediator of integrin mechanosensing. This dual role distinguishes talin from kindlins, which are also critical for integrin activation but do not seem to mediate a direct connection to the actin cytoskeleton³⁸.

Intriguingly, integrin-dependent mechanosensing is talin isoform specific (Fig. 6). Although our data are consistent with the previously proposed tension-dependent vinculin recruitment to talin-1's N-terminal rod domain^{15,29–31}, this mechanism does not seem to exist for talin-2. Instead, vinculin recruitment occurs even in the absence of C-terminal F-actin binding, which coincides with increased talin-2 FA immobilization and elevated average tension levels. As a consequence, talin-2-expressing cells spread more efficiently on 1–2 kPa surfaces than their talin-1 counterparts and it is interesting to note that talin-2 is expressed highest in brain tissue, which is characterized by similar rigidities^{32,39}. In our experiments, the observed mechanical differences can be ascribed to talin's R1–R3 domains (Fig. 7), which seemingly contrasts a previous study that attributed isoform-specific differences to distinct integrin–talin head-domain affinities⁴⁰. It has to be noted, however, that the *Tln1*^{-/-}/*Tln2*^{-/-} cells used here do not express integrin $\beta_1 D$, a muscle-specific integrin isoform for which especially high affinities to talin-2 have been reported⁴⁰. Thus, a study using muscle-specific cell types or genetically modified cell lines expressing distinct integrin receptor subtypes is needed.

Collectively, our experiments reveal that talins mediate a mechanical linkage that is essential for coupling cell adhesion with integrin mechanosensing and is thus required for cells to detect tissue stiffness. It seems that differential expression of talin isoforms provides a means by which cells adjust to different ECM rigidities and the fact that integrins and at least one talin isoform are abundantly expressed in all cell types indicates that the observed mechanical linkages are relevant in many tissues. As tissue rigidity changes during development or with the onset of numerous disease states^{1–4,6}, it will be important to investigate the role of the individual talin isoforms during these processes in more detail. The biosensors described in this study will allow the isoform-specific analysis of talin force transduction in many cell types and should be useful for such studies. Furthermore, they will be valuable to investigate effects of other talin interaction partners, such as RIAM or FAK, on molecular force propagation in FAs. Finally, application of the HP35 probes to other force-transducing proteins should allow the detailed analysis of many different mechanobiological processes that are subject to higher single piconewton forces in cells and whole organisms. □

METHODS

Methods and any associated references are available in the online version of the paper.

Note: Supplementary Information is available in the online version of the paper

ACKNOWLEDGEMENTS

C.G. is supported by the German Research Council (DFG, GR3399/2-1 and GR3399/5-1), the Collaborative Research Centre SFB863 (B9) and a Paul Gerson Unna Research Group of the Max Planck Förderstiftung. A.M. is supported by the Nanosystems Initiative Munich (NIM). M.R. is supported by the German Research Council through the Collaborative Research Centre SFB863 (A2). R.Z. is supported by R01-DK083187, R01-DK075594, R01-DK069221 and VA Merit Award

II01BX002196. B.S. acknowledges financial support from the DAAD. The authors thank R. Fässler for continuous support and helpful discussions; F. Schnorrer for critically reading the manuscript; A. Lambacher and the MPIB core facility for technical support; G. Zoldak for helpful discussion, A. Sechi for sharing data analysis software and D. Critchley (University of Leicester, UK) for providing talin-2 cDNA.

AUTHOR CONTRIBUTIONS

C.G. and K.A. initiated the project, generated cell lines, performed cellular and biochemical experiments and analysed data; P.R. generated cell lines, performed cellular experiments, wrote data analysis software and analysed data. A.M. and M.R. performed the single-molecule calibration and theoretical modelling. A.C.-G. created talin expression constructs, C.Kluger generated vinculin expression constructs and cell lines, C.Kluger and C.Klingner wrote data analysis software. K.A., C.Kluger and B.S. performed traction force microscopy experiments and analyses. R.Z. provided genetically modified talin cells. C.G. wrote the manuscript with the input from all authors. K.A., P.R. and A.M. contributed equally.

COMPETING FINANCIAL INTERESTS

The authors declare no competing financial interests.

Published online at <http://dx.doi.org/10.1038/ncb3268>

Reprints and permissions information is available online at www.nature.com/reprints

- Heisenberg, C. P. & Bellaïche, Y. Forces in tissue morphogenesis and patterning. *Cell* **153**, 948–962 (2013).
- Wozniak, M. A. & Chen, C. S. Mechanotransduction in development: a growing role for contractility. *Nat. Rev. Mol. Cell Biol.* **10**, 34–43 (2009).
- Franze, K., Janmey, P. A. & Guck, J. Mechanics in neuronal development and repair. *Annu. Rev. Biomed. Eng.* **15**, 227–251 (2013).
- Ingber, D. E. Mechanobiology and diseases of mechanotransduction. *Ann. Med.* **35**, 564–577 (2003).
- Lu, P., Takai, K., Weaver, V. M. & Werb, Z. Extracellular matrix degradation and remodeling in development and disease. *Cold Spring Harb. Perspect. Biol.* **3**, <http://dx.doi.org/10.1101/cshperspect.a05058> (2011).
- Discher, D. E., Janmey, P. & Wang, Y. L. Tissue cells feel and respond to the stiffness of their substrate. *Science* **310**, 1139–1143 (2005).
- Plotnikov, S. V., Pasapera, A. M., Sabass, B. & Waterman, C. M. Force fluctuations within focal adhesions mediate ECM-rigidity sensing to guide directed cell migration. *Cell* **151**, 1513–1527 (2012).
- Schoen, I., Pruitt, B. L. & Vogel, V. The Yin-Yang of rigidity sensing: how forces and mechanical properties regulate the cellular response to materials. *Annu. Rev. Mater. Res.* **43**, 589–618 (2013).
- Geiger, B., Spatz, J. P. & Bershadsky, A. D. Environmental sensing through focal adhesions. *Nat. Rev. Mol. Cell Biol.* **10**, 21–33 (2009).
- Hoffman, B. D., Grashoff, C. & Schwartz, M. A. Dynamic molecular processes mediate cellular mechanotransduction. *Nature* **475**, 316–323 (2011).
- Elosegi-Artola, A. et al. Rigidity sensing and adaptation through regulation of integrin types. *Nat. Mater.* **13**, 631–637 (2014).
- Grashoff, C. et al. Measuring mechanical tension across vinculin reveals regulation of focal adhesion dynamics. *Nature* **466**, 263–266 (2010).
- Kanchanawong, P. et al. Nanoscale architecture of integrin-based cell adhesions. *Nature* **468**, 580–584 (2010).
- del Rio, A. et al. Stretching single talin rod molecules activates vinculin binding. *Science* **323**, 638–641 (2009).
- Liu, J. et al. Talin determines the nanoscale architecture of focal adhesions. *Proc. Natl Acad. Sci. USA* **112**, E4864–E4873 (2015).
- Austen, K., Kluger, C., Freikamp, A., Chrostek-Grashoff, A. & Grashoff, C. Generation and analysis of biosensors to measure mechanical forces within cells. *Methods Mol. Biol.* **1066**, 169–184 (2013).
- Cost, A. L., Ringer, P., Chrostek-Grashoff, A. & Grashoff, C. How to measure molecular forces in cells: a guide to evaluating genetically-encoded FRET-based tension sensors. *Cell. Mol. Bioeng.* **8**, 96–105 (2015).
- Guo, J., Sachs, F. & Meng, F. Fluorescence-based force/tension sensors: a novel tool to visualize mechanical forces in structural proteins in live cells. *Antioxid. Redox Signal.* **20**, 986–999 (2014).
- Finer, J. T., Simmons, R. M. & Spudich, J. A. Single myosin molecule mechanics: piconewton forces and nanometre steps. *Nature* **368**, 113–119 (1994).
- Wang, X. & Ha, T. Defining single molecular forces required to activate integrin and notch signalling. *Science* **340**, 991–994 (2013).
- Blakely, B. L. et al. A DNA-based molecular probe for optically reporting cellular traction forces. *Nat. Methods* **11**, 1229–1232 (2014).
- Duan, Y. & Kollman, P. A. Pathways to a protein folding intermediate observed in a 1-microsecond simulation in aqueous solution. *Science* **282**, 740–744 (1998).
- Zoldak, G., Stigler, J., Pelz, B., Li, H. & Rief, M. Ultrafast folding kinetics and cooperativity of villin headpiece in single-molecule force spectroscopy. *Proc. Natl Acad. Sci. USA* **110**, 18156–18161 (2013).

TECHNICAL REPORT

25. Zhang, X. *et al.* Talin depletion reveals independence of initial cell spreading from integrin activation and traction. *Nat. Cell Biol.* **10**, 1062–1068 (2008).
26. Carisey, A. *et al.* Vinculin regulates the recruitment and release of core focal adhesion proteins in a force-dependent manner. *Curr. Biol.* **23**, 271–281 (2013).
27. Dumbauld, D. W. *et al.* How vinculin regulates force transmission. *Proc. Natl Acad. Sci. USA* **110**, 9788–9793 (2013).
28. Humphries, J. D. *et al.* Vinculin controls focal adhesion formation by direct interactions with talin and actin. *J. Cell Biol.* **179**, 1043–1057 (2007).
29. Hytonen, V. P. & Vogel, V. How force might activate talin's vinculin binding sites: SMD reveals a structural mechanism. *PLoS Comput. Biol.* **4**, e24 (2008).
30. Yao, M. *et al.* Mechanical activation of vinculin binding to talin locks talin in an unfolded conformation. *Sci. Rep.* **4**, 4610 (2014).
31. Ciobanaru, C., Faivre, B. & Le Clainche, C. Actomyosin-dependent formation of the mechanosensitive talin–vinculin complex reinforces actin anchoring. *Nat. Commun.* **5**, 3095 (2014).
32. Praekelt, U. *et al.* New isoform-specific monoclonal antibodies reveal different sub-cellular localisations for talin1 and talin2. *Eur. J. Cell Biol.* **91**, 180–191 (2012).
33. Borghi, N. *et al.* E-cadherin is under constitutive actomyosin-generated tension that is increased at cell–cell contacts upon externally applied stretch. *Proc. Natl Acad. Sci. USA* **109**, 12568–12573 (2012).
34. Krieg, M., Dunn, A. R. & Goodman, M. B. Mechanical control of the sense of touch by β-spectrin. *Nat. Cell Biol.* **16**, 224–233 (2014).
35. Paszek, M. J. *et al.* The cancer glycocalyx mechanically primes integrin-mediated growth and survival. *Nature* **511**, 319–325 (2014).
36. Cai, D. *et al.* Mechanical feedback through E-cadherin promotes direction sensing during collective cell migration. *Cell* **157**, 1146–1159 (2014).
37. Conway, D. E. *et al.* Fluid shear stress on endothelial cells modulates mechanical tension across VE-cadherin and PECAM-1. *Curr. Biol.* **23**, 1024–1030 (2013).
38. Moser, M., Legate, K. R., Zent, R. & Fassler, R. The tail of integrins, talin, and kindlins. *Science* **324**, 895–899 (2009).
39. Miller, K., Chinzei, K., Orsengo, G. & Bednarz, P. Mechanical properties of brain tissue *in-vivo*: experiment and computer simulation. *J. Biomech.* **33**, 1369–1376 (2000).
40. Anthis, N. J., Wegener, K. L., Critchley, D. R. & Campbell, I. D. Structural diversity in integrin/talin interactions. *Structure* **18**, 1654–1666 (2010).

METHODS

Antibodies and reagents. The following antibodies were used: anti-paxillin (clone 349; BD Transduction Laboratories, 610051; immunofluorescence (IF) 1:400), anti-talin-1 (C45F1; Cell Signaling, 4021; western blotting (WB) 1:1,000), anti-talin-1/2 (8d4; Sigma, T3287; WB 1:2,000), anti-talin-2 (68E7; Abcam, ab105458; WB 1:2,000), anti-vinculin (hVIN-1; Sigma, V9131; WB 1:4,000 and IF 1:200), anti-tubulin (DM1A; Sigma, T9026; WB 1:3,000), anti-FAK (Millipore, 06-543; WB 1:2,000 and IF 1:200), anti-pY397-FAK (Life Technologies, 44-624; WB 1:1,000), anti-kindlin2 (Millipore, MAB2617; IF 1:400), anti-GFP (Abcam, ab290; WB 1:2,000), anti- β_1 integrin (Chemicon, MAB1997; FACS 1:400 and IF 1:200), anti- β_1 integrin (9EG7; PharMingen, 550531; FACS 1:200 and IF 1:200), anti-mouse IgG-horseradish peroxidase (HRP) conjugate (Bio-Rad, 170-6516; WB 1:15,000), anti-rabbit IgG-HRP conjugate (Bio-Rad, 170-6515; WB 1:15,000), anti-mouse IgG-Alexa Fluor-405 (Life Technologies, A31553; IF 1:400), anti-mouse IgG-Alexa Fluor-647 (Life Technologies, A31571; IF 1:400), anti-rat IgG-Alexa Fluor-647 (Life Technologies, A21247; IF 1:400). The following reagents were used: Alexa Fluor-568 phalloidin (Life Technologies, A12380; IF 1:400), Alexa Fluor-647 phalloidin (Life Technologies, A22287; IF 1:400), poly-L-lysine (Sigma, P4707), puromycin (Sigma, P8833), Y-27632 (Sigma, Y0503), fibronectin (Calbiochem, 341631). Micro-patterned substrates (CYTOO) and Softview Easy Coat 0.2, 0.5, 1.0, 2.0, 4.0, 12 and 25 kPa soft substrate dishes (Matrigen Life Technologies) were used.

Generation of HP35-TS cDNA expression constructs. HP35-TS cDNA constructs were generated according to our published protocols¹⁷. In brief, restriction sites were added to YPet (amino acids (aa) 1–228) (5'Xho/3'BamHI) and mCherry (5'BamHI/3'NotI) cDNA by polymerase chain reaction (PCR) and PCR products were combined in a pBluescript SK(+) vector. The sequence encoding for the HP35 linker peptide (LSDEDFKAVFGMTRSAFANPLWKQQNLKKEKGLF) was inserted between fluorophores using annealed oligonucleotides with 5'BglII/3'BamHI overhangs (forward primer: 5'-aat tca gat ctC TCT CCG ATG AGG ACT TCA AAG CTG TGT TTG GCA TGA CCA GGA GCG CAT TTG CCA ACC TTC CTC TGT GGA AAC AGC AAC ACC TGA AGA AGG AAA AGG GAC TGT TCg-3'; reverse primer: 5'-gat ccG AAC AGT CCC TTT TCC TTC TCA AGG TGT TGC TGT TTC CAC AGA GGA AGG TTG GCA AAT GCG CTC CTG GTC ATG CCA AAC AAC GCT TTG AAG TCC TCA TCG GAG AGA gat ctg-3'). The TS module containing the stable HP35st linker peptide (LSDEDFKAVFGMTRSAFANPLWKQQALMKKEKGLF) was created using the QuikChange II Site-Directed Mutagenesis kit (Agilent Technologies). For expression in cells, HP35(st)-TS cDNA was transferred into the pLPCX plasmid (Clontech) containing a modified multiple cloning site (pLPCXmod). To modify HP35(st)-TS for single-molecule calibration (smHP35-TS and smHP35st-TS), terminal cysteine residues to allow attachment of DNA oligonucleotides and a histidine-tag for protein purification were added by PCR; the cDNA was then transferred into pLPCXmod. The correct sequence of all constructs was confirmed by DNA sequencing (Eurofins Genomics).

Protein expression and purification. For protein expression, smHP35-TS or smHP35st-TS was transiently transfected into HEK293 cells by CaPO₄-precipitation as described before¹⁷. After 48 h, cells were detached, re-suspended in hypotonic lysis buffer, incubated for 20 min on ice and then homogenized with a Dounce homogenizer. Lysates were cleared by centrifugation and subjected to metal ion affinity chromatography (His-Trap, GE Healthcare), followed by ion-exchange chromatography (Sephadex, GE Healthcare). Purified samples were then concentrated to about 20 μ M by membrane ultrafiltration (Vivaspin, GE Healthcare) and subjected to the protein–oligonucleotide binding reaction described below.

Assembling protein–DNA chimaeras. To attach DNA handles to smHP35-TS or smHP35st-TS, cysteine-based chemistry was used according to previously published protocols^{41,42}. In brief, 34 base pair-long, lyophilized maleimide-modified single-stranded (ss) DNA oligonucleotides were dissolved in phosphate buffered saline (PBS, pH 6.7) and incubated overnight at 4 °C with the purified protein; the protein was kept in PBS supplemented with 0.2 mM Tris-2-carboxyethylphosphine (TCEP) to avoid oligomerization through disulphide bonds. By-products, namely unreacted oligonucleotides, unreacted protein and protein with only one attached DNA handle, were removed using metal ion affinity chromatography (His-Trap, GE Healthcare) in combination with size-exclusion chromatography (Superdex 200, GE Healthcare). Finally, double-stranded (ds) DNA (λ -DNA, NEB) handles, carrying a biotin modification or a digoxigenin modification at one end and a ss-overhang at the other, were hybridized to complementary ssDNA oligonucleotides at either end of the protein resulting in a contour length of 185 nm for each handle.

Optical tweezers set-up, sample preparation and measurement procedure. To calibrate the new HP35(st)-TS biosensors, we performed single-molecule force spectroscopy measurements using a custom-built, dual-trap optical tweezers set-up

with back-focal plane detection as described previously⁴³; for improved temporal resolution, quadrant photodiodes were used as position-sensitive devices (QP154-Q-HVSD, Pacific Silicon Sensor). Data on the beads' positions with respect to their trap centres as well as the distance between the two traps were sampled at 200 kHz and filtered at the Nyquist frequency. Each trap's signal was corrected for cross-talk; trap stiffnesses calculated from corrected power spectra were determined to be about 0.37 pN nm⁻¹; the error of the trap stiffness calibration is approximately 10%. To prepare the sample, streptavidin-coated 1 μ m-sized silica beads (Bangs Laboratories) were incubated with protein–DNA chimaeras in PBS (pH 7.4). Next, functionalized anti-digoxigenin silica beads were added; glucose oxidase and catalase were used as an oxygen scavenger system (26 U ml⁻¹ glucose oxidase, 1,700 U ml⁻¹ catalase, and 0.6% (w/v) glucose)^{41,42}. To obtain the dumbbell-like configuration schematically shown in Fig. 1b, one anti-digoxigenin and one streptavidin-functionalized bead were trapped, each in one of the two laser foci of the dual trap. By moving the laser beam of one steerable laser focus, both beads were brought in close proximity until a single tether was successfully formed. Subsequently, repeated stretch-and-relax cycles were performed at constant velocities of 10–500 nm s⁻¹. Each cycle yielded typical force–extension traces where protein unfolding and refolding could be observed. Keeping the traps at constant distance allowed us to record time traces of protein fluctuations at constant force bias; maximal forces of about 50 pN were reached. A step-by-step protocol describing the biosensor calibration can be found at Nature Protocol Exchange⁴⁴.

HP35-TS and HP35st-TS force–extension relation. To generate force–extension calibration curves (Fig. 1i, dashed lines), we converted our force–distance measurements and complete fits to the data into corresponding force–extension curves (Supplementary Note). The gain in extension caused by the dsDNA handles was subtracted using the parameters supplied by the extensible worm-like chain fit (eWLC-fit; see Supplementary Note) so that the remaining force–extension relation is characteristic for HP35(st)-TS and the thermal motion of the system. By averaging multiple smoothed force–extension traces of one single molecule, sub-nanometre resolution was obtained (Fig. 1d, squares).

Evaluating the mechanical stability of genetically encoded fluorophores. Fluorophore stability is critical to any FRET-based force sensor as unfolding of donor or acceptor fluorophore would prohibit quantitative measurements. We therefore set up experiments to specifically examine HP35-TS fluorophore stability under force. As expected, fluorophore unfolding occurred only if at least 35 pN were reached/exceeded during pulling measurements (pulling velocity: 500 nm s⁻¹; Fig. 1e). To examine fluorophore stability under constant force, we exposed HP35-TS to 24 pN for more than 5 min but also did not observe any fluorophore unfolding (Fig. 1f). We also note that the observed average contour length of 363 nm was actually less than the expected theoretical 370 nm for both handles (Supplementary Note) indicating that both fluorophores are properly folded in HP35-TS. Altogether, these experiments suggest that the employed fluorophores in HP35-TS are insensitive to the mechanical forces the biosensors are supposed to measure.

Generation of talin expression constructs. Talin-1 expression constructs are based on murine talin-1 cDNA (accession number: X56123). To generate C-terminal fusion constructs (Tln1Y, Tln1C and Tln1Con), restriction sites (5'EcoRI/3'NotI) along with 5' Kozak-sequence (ACC ATG) were added and the 3' stop codon was removed by PCR. In parallel, restriction sites (5'NotI/3'ClaI) and stop codon were added to YPet, mCherry or HP35-TS cDNA by PCR and these fragments were combined with talin cDNA using NotI/ClaI restriction sites. For transient or stable expression in cells, constructs were cloned into pLPCXmod. To insert individual fluorophores (Tln1Y-i, Tln1C-i) or tension sensors into talin-1, we generated a short linker encoding for 5'Sall/3'NotI restriction sites after the codon corresponding to aa 447 in murine talin-1 cDNA by overlap extension PCR; cDNAs of the individual fluorophores or the HP35-TS were inserted using 5'Xho/3'NotI restriction sites. Point mutations (M319A, K324D) were introduced into talin-1 cDNA using the QuikChange II Site-Directed Mutagenesis kit (Agilent Technologies); deletion mutants (Tln1-2300 and Tln1-950) were generated by PCR amplification of the respective cDNA fragments. As we had access only to human talin-2 cDNA, we generated expression constructs based on human talin-1 (BC042923) and human talin-2 (NM015059) to allow a direct comparison of both isoforms. On the basis of aa homology, HP35-TS(st) was inserted into talin-2 after the codon corresponding to aa 450. In the chimaeric talin-1/2 constructs, the talin-1 head domain (aa 1–447) was fused to the talin-2 rod domain (aa 451–2,542); in the talin-2/1 construct, the talin-2 head domain (aa 1–450) was fused to the talin-1 rod domain (aa 448–2,541). To delete domains R1–R3, sequences corresponding to aa 482–911 for talin-1 and aa 485–914 for talin-2 were removed.

Generation of vinculin and RhoA cDNA expression constructs. To generate vinculin expression constructs, human full-length vinculin cDNA was isolated from an ImaGene cDNA library (BG284191) and 5'Apal/3'XbaI restriction sites as well as a Kozak sequence were added by PCR; also the vinculin truncation mutant (encoding for aa 1–883) was amplified by PCR. A TagBFP-fluorophore was added C-terminally to each construct using 5'XhoI/3'NotI (vinculin truncation mutant) or 5'XbaI/3'NotI (full-length vinculin) restriction sites, and the final cDNAs were transferred into a pLPCXmod by 5'Apal/3'NotI. The active RhoA expression construct was based on a previously described EGFP-tagged RhoQ63L cDNA (ref. 45). To allow fluorescence analysis in the presence of YPet-tagged talin-1 constructs, the N-terminal EGFP was exchanged for TagBFP using 5'HindIII/3'EcoRI restriction sites.

Generation of talin- and vinculin-deficient cell lines and stable protein re-expression. To generate cells in which both talin-1 and talin-2 are genetically inactivated, talin-2 knockout mice (*Tln2*^{-/-}; ref. 46) were intercrossed with mice in which the talin-1 gene is flanked with loxP sites (*Tln1*^{fl/fl}; ref. 47). Mice with the *Tln1*^{fl/fl}/*Tln2*^{-/-} genotype were used to isolate fibroblastoid cells from kidneys of a three-week-old mouse and cells were subsequently immortalized with the SV40 large T antigen. Talin-1 was abrogated by adenoviral transduction of Cre recombinase and clonal cell lines were isolated. To generate vinculin-deficient cells, SV40 large T immortalized fibroblasts, in which the vinculin gene is flanked with loxP sites (*Vin*^{fl/fl}), were transduced with Cre recombinase and clonal cell lines were isolated (*Vin*^{-/-}). Vinculin cDNA constructs were transiently transduced using Lipofectamine 2000 (Invitrogen) and talin double knockout cells (*Tln1*^{-/-}/*Tln2*^{-/-}) were stably transduced by the phoenix cell transfection system as described earlier⁴⁷. After infection, cells were puromycin-selected and stable protein expression was confirmed by western blotting using standard protocols. When necessary, cells were sorted by fluorescence-activated cell sorting (FACS) using a FACSaria cell sorter IIU (BD Biosciences) to isolate cells with comparable expression levels. Cell lines were freshly generated for this work and thus are not listed in the database of commonly misidentified cell lines maintained by ICLAC and NCBI Biosample; the cell lines have not been authenticated.

Cell culture conditions and immunostaining protocol. Cell lines were cultured in high-glucose DMEM-GlutaMAX medium (Life Technologies) supplemented with 10% fetal bovine serum (FBS, Life Technologies) and 1% penicillin/streptomycin (P/S, Life Technologies; growth medium). For live-cell imaging, DMEM without phenol red containing 4.5 mg ml⁻¹ glucose, 25 mM HEPES, 2 mM glutamine (Life Technologies) was used and supplemented with 10% FBS and 1% P/S (imaging medium). For cell staining, cells were seeded on FN-coated (10 µg ml⁻¹) glass slides (Menzel, no. 1.5) and allowed to spread overnight, if not indicated otherwise. Cells were fixed in 4% paraformaldehyde (PFA) for 10 min at room temperature and immunostainings were performed as described before⁴⁷. Samples were mounted in Prolong Gold (Life Technologies) and stored at 4 °C. Images were acquired using a LSM780 confocal scanning microscope equipped with a 100× oil objective (Plan-APOCHROMAT, NA = 1.46). For image acquisition of cells on soft substrates, a Leica TCS SP5 X confocal microscope equipped with a 40× long-distance water objective (APO 40×/1.10 W CORR C S2) was used.

Fluorescence-activated cell sorting (FACS). Integrin surface expression was determined by FACS using a BD FACS Canto II instrument (BD Biosciences). Cell stainings with anti-integrin antibodies were performed in 5% BSA solution containing 1 mM MgCl₂, 1 mM CaCl₂ and 0.02% NaN₃. To control for unspecific antibody labelling, cells lacking β₁, β₂, β₃ and β₇ integrin subunits were used⁴⁸. Surface expression of integrins was quantified by geometric mean fluorescence intensity using FlowJo software (Tree Star).

Fluorescence recovery after photobleaching (FRAP) experiment and analysis. To allow FRAP analysis of cells with comparable FA sizes and states, cells were seeded on FN-coated micro-patterned substrates (CYTOO); under these conditions, cells adapt highly similar morphologies and develop very regular FAs of comparable size, shape and intensity. For each experiment, Tln1Y, Tln2Y and Tln1TS cells were seeded on Y-shaped micro-patterned substrates for at least 4 h and were analysed at 37 °C and 5% CO₂ on a Leica SP8 confocal laser scanning microscope equipped with a 63× water objective (HCX PL APO, NA = 1.2). Cells of comparable intensity were excited at 514 nm with a laser power of 5% to record two pre-bleach images within an interval of 10 s. Selected FAs were then photobleached using a laser power of 100% for 1 s and post-bleach images were acquired every 20 s for 260–280 s; the fluorescence intensity was recorded between 530–570 nm. Next, fluorescence intensity data were imported into ImageJ and analysed using the ImageJ plugin ‘FRAP profiler’. Only data with comparable initial mean intensities and sufficient initial photobleaching were processed in MATLAB (Mathworks). To determine fluorescence recovery, we assumed a reaction-dominated model as described before^{49,50} and fitted the data

according to equation (1). Only data sets with a fitting quality of $R^2 = 0.98$ were considered for further analysis.

$$f(t) = A(1 - e^{-k_{\text{off}}t}) \quad (1)$$

where t is time, k_{off} is the rate constant and A is the mobile fraction. The recovery half-time $\tau_{1/2}$ was calculated according to equation (2).

$$\tau_{1/2} = \frac{\ln(2)}{k_{\text{off}}} \quad (2)$$

Time-correlated single-photon counting fluorescence lifetime microscopy (TCSPC-FLIM). TCSPC-FLIM experiments were performed using a confocal microscope (Leica TCS SP5 X) equipped with a pulsed white light laser (WLL, 80 MHz repetition rate, NKT Photonics), a FLIM X16 TCSPC detector (LaVision Biotec) and a 63× water objective (HCX PL APO CS, NA = 1.2); a band-pass filter 545/30 (AHF Analysetechnik) was used to block photons emitted by the acceptor fluorophore. Images were acquired with a scanning velocity of 400 Hz, a spatial resolution of 512 × 512 pixels and resulting image field coverage of 123.02 × 123.02 µm². The detection covered a time window of 12.24 ns after the excitation pulse with a temporal resolution of 0.08 ns. For each experimental condition 15–20 cells were recorded and each experiment was repeated at least 3–5 times. Data analysis was conducted by a custom-written MATLAB program calculating the FRET efficiency E according to equation (3), where τ_D is the mean donor lifetime and τ_{DA} is the lifetime of the donor in the presence of an acceptor fluorophore. For more detailed information see our previously published protocols¹⁷.

$$E = 1 - \frac{\tau_{DA}}{\tau_D} \quad (3)$$

Measurement of fluorophore emission spectra in FAs of living cells. To examine whether the photo-physical properties of the donor or acceptor fluorophore are affected by their insertion into talin, *Tln1*^{-/-}/*Tln2*^{-/-} cells were reconstituted with constructs in which the individual fluorophores had been inserted into talin-1 (Tln1Y-i, Tln1C-i) or were C-terminally attached (Tln1Y, Tln1C). Cells were seeded on FN-coated coverslips and the emission spectra of integrated or C-terminally tagged fluorophores from FAs of living cells were measured. The emission spectra of YPet (excitation: 508 nm; detection: 525–605 nm; 10 nm detection band width) and mCherry (excitation: 587 nm; detection: 610–710 nm; 20 nm detection band width) were recorded using a confocal microscope equipped with an acousto-optical beamsplitter (Leica TCS SP5 X) and a pulsed white light laser (WLL, 80 MHz repetition rate, NKT Photonics). Only FA-specific signal was processed in the subsequent data analysis.

FRET control experiment I—effects of intermolecular FRET. To test for effects of intermolecular FRET (that is, energy transfer between adjacent molecules), *Tln1*^{-/-}/*Tln2*^{-/-} cells were co-transfected with constructs in which the individual fluorophores were inserted into talin-1 or C-terminally attached. These cells were then seeded on FN- or pL-coated glass slides and FRET efficiencies were determined using TCSPC-FLIM. We did not observe differences when pL and FN conditions were compared indicating that effects of intermolecular FRET in these experiments are negligible. However, a slight increase of intermolecular FRET in C-terminally tagged talin controls was detectable, presumably due to talin dimerization that is mediated at talin's C terminus (Fig. 2g); this may explain the slightly increased FRET efficiency values determined in Tln1Con cells as compared with Tln1TS cells on pL (for example, Fig. 2i).

FRET control experiment II—effects of talin's inter-domain association. To examine whether Tln1TS FRET is affected by the inter-domain association between the talin head and the talin rod domains⁵¹, we inserted point mutations (K324D and M319A) into Tln1TS that were previously described to abolish the intramolecular interaction^{51,52}. As talin is expected to predominantly exist in an auto-inhibited conformation in the cytoplasm⁵³, we reasoned that the high FRET efficiencies observed in cells on pL should be significantly reduced by these activating point mutations if FRET of the biosensor was sensitive to conformational changes. However, FRET efficiencies of Tln1TS-M319A, Tln1TS-K324D and Tln1TS were indistinguishable when cells were seeded on pL (Fig. 2h). This indicates that effects of the inter-domain association on Tln1TS FRET are negligible.

FRET control experiment III—evaluating effects of fluorescence intensity and temperature. To examine whether the observed FRET effects are fluorescence intensity dependent, FRET efficiencies were plotted over mean fluorescence intensities and the Pearson's correlation coefficient (PCC) was determined (Supplementary Fig. 2c); however, no correlation was observed. As HP35 unfolding shows a small but significant temperature dependency (see Supplementary Note and Supplementary Fig. 1i) we also tested how moderate changes in temperature affect FRET measurements. Thus, FRET ratio measurements of Tln1Con or Tln1TS cells

were performed at 30 °C (the temperature at which the single-molecule calibration was performed) and 37 °C (the temperature used during FRET ratio measurements; Supplementary Fig. 2d).

Isolating FA-specific signals for FLIM and ratiometric FRET analysis. To isolate the FA-specific signals from FLIM data sets, images were imported into MATLAB and regions of interest (ROIs) were manually set to exclude cytoplasmic background and signals from adjacent cells. A three-level multi-Otsu thresholding algorithm was applied and the highest intensities were defined as FA signal. After conversion into a binary image, these FA masks were used to calculate the mean FA FRET efficiency per cell. To isolate FA signals for morphological analysis and ratiometric FRET measurements, fluorescence images were imported to MATLAB followed by manual ROI selection to analyse individual cells. Cytosolic background was subtracted from the donor image by convolving the image (Gaussian structure element; width: 25, height: 2) and applying a top-hat filtering step (disk structure element; radius: 7 pixel) as described before⁵⁴. Obtained individual FA masks were then used to calculate FA mean intensity of donor and acceptor signal. For mean acceptor values 1.7 times larger than manually determined average background signal, individual FA ratiometric FRET values were calculated by mean intensity acceptor/donor division. Step-by-step protocols describing the live-cell FLIM and FRET experiments can be found at Nature Protocol Exchange⁴⁴.

Morphological FA analysis and FA co-localization analysis. For cell size and polarization analysis, cells were allowed to spread on FN-coated glass coverslips or on FN-coated Softview Easy Coat dishes (Matrigen Life Technologies). At the indicated time points, cells were fixed and stained. Images of phalloidin-stained cells were then used to determine the cell area and the cell's major principal axis. Using Otsu thresholding as a cutoff criterion, binarized cellular shape masks were created and mask orientation was calculated to define the reference major principal axis. Subsequently, individual FA masks were analysed with respect to their eccentricity and area. The FA orientation with respect to cell major principal axis was used to evaluate cell polarization. To quantify subcellular co-localization of vinculin with talin, cells were fixed and immunostained for vinculin as described above. Intensity line plots across at least 25 FAs were defined in ImageJ and evaluated in MATLAB. To find the local maximum of individual FAs, a Gaussian fit was applied in the talin channel. Intensity values for both channels at the fitted maximum ± 2 pixels were averaged to minimize local errors.

Traction force microscopy. Traction force microscopy was performed using an SP8 confocal laser scanning microscope equipped with a 63× glycerol objective (HC PL APO, NA = 1.3). Fluorescent beads of 0.2 μm diameter (FluoSpheres (625/645), Life Technologies) were incorporated into polyacrylamide gels with defined elastic properties that were produced according to established protocols⁵⁵. Young's moduli of the substrates were calculated from acrylamide/bis-acrylamide concentrations as previously described⁵⁶ and obtained moduli were checked by measuring the indentation profile of a coloured bead that was placed on the gel surface as described in ref. 57; the analysis of traction force microscopy data was performed as described before⁵⁸.

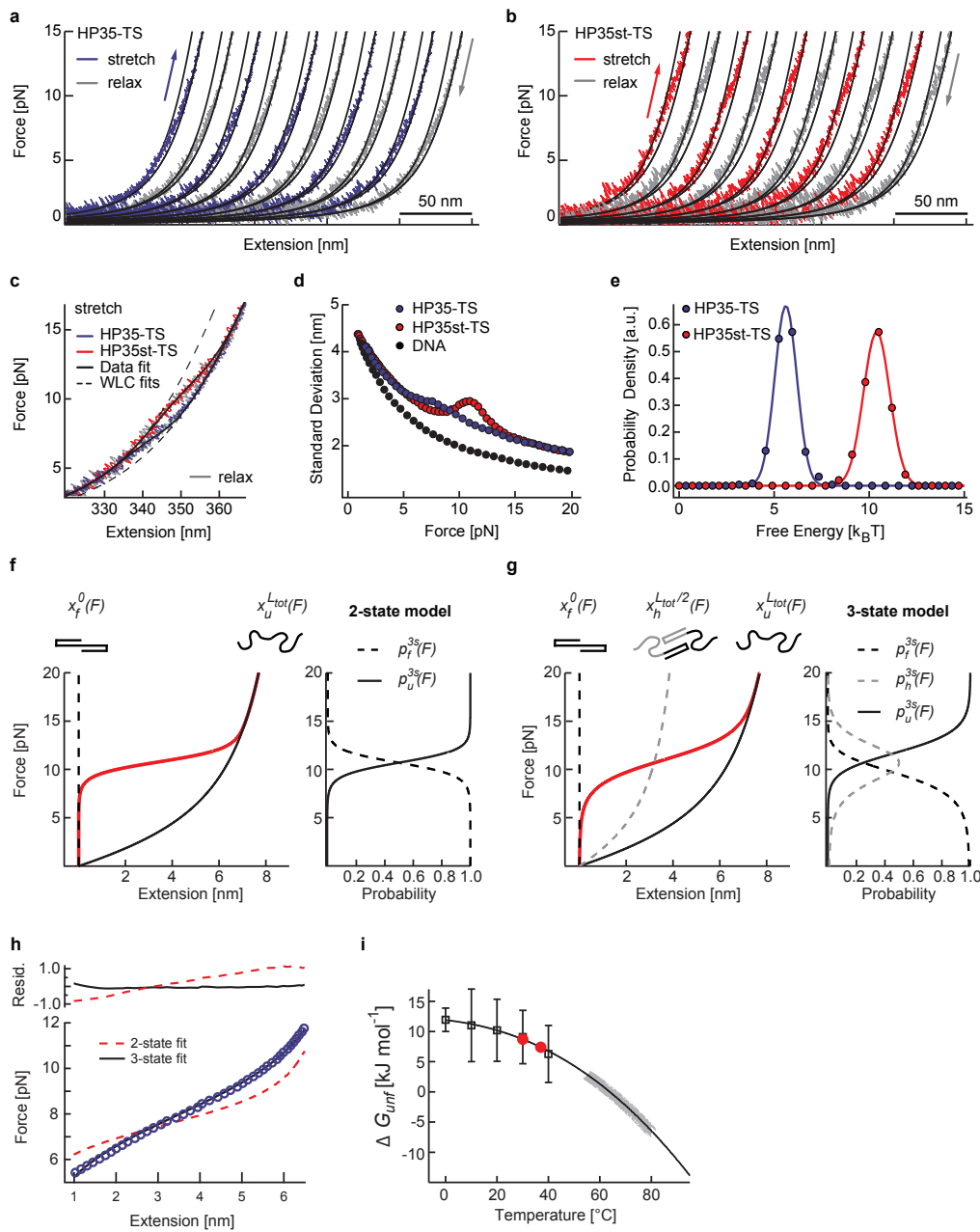
Sources of noise and data interpretation. Live-cell FRET experiments are inherently noisy because the energy transfer rate between the donor and acceptor fluorophore does not depend only on the fluorophore separation distance but also on other factors^{18,59} including temperature, pH or ion concentration. Furthermore, targeting a biosensor to a specific subcellular location can further complicate the experiment as effects through intermolecular FRET or molecular crowding may become more prominent. In addition, the biosensor expression level and the used cell type, in particular potentially high expression levels of the endogenous protein, need to be taken into account. Finally, chromatic aberrations, laser fluctuations, the Poisson statistics of photon arrival at the detector or other technical limitations contribute to the noise in FRET measurements. It is also important to note that in contrast to the single-molecule calibration experiments described in Fig. 1, the live-cell FRET experiments presented in Figs 2–4 and Figs 6 and 7 are based on bulk measurements, in which the signal from hundreds of FAs containing many molecules is averaged to calculate a mean FRET

efficiency per cell. As a consequence, only an average force per molecule can be calculated.

Statistical analyses. Error bars represent the standard error of the mean (s.e.m.) if not indicated otherwise; to confirm that data are normally distributed, the Lilliefors test was used. Statistical significance is given by a *P* value calculated from a two-sample Kolmogorov-Smirnov test using the default significance level of $\alpha = 0.05$. Additional testing was performed with a two-sided *t*-test as indicated. The following nomenclature was used in all figures: ***, *P* < 0.001; **, *P* < 0.01; *, *P* < 0.05; not significant (NS), *P* > 0.05. Box plots were generated using the MATLAB function box plot() or the origin Lab software indicating the median as well as 25th and 75th percentiles; whiskers reach out to 2.7 standard deviations (σ). Statistic source data are available in Supplementary Table 1.

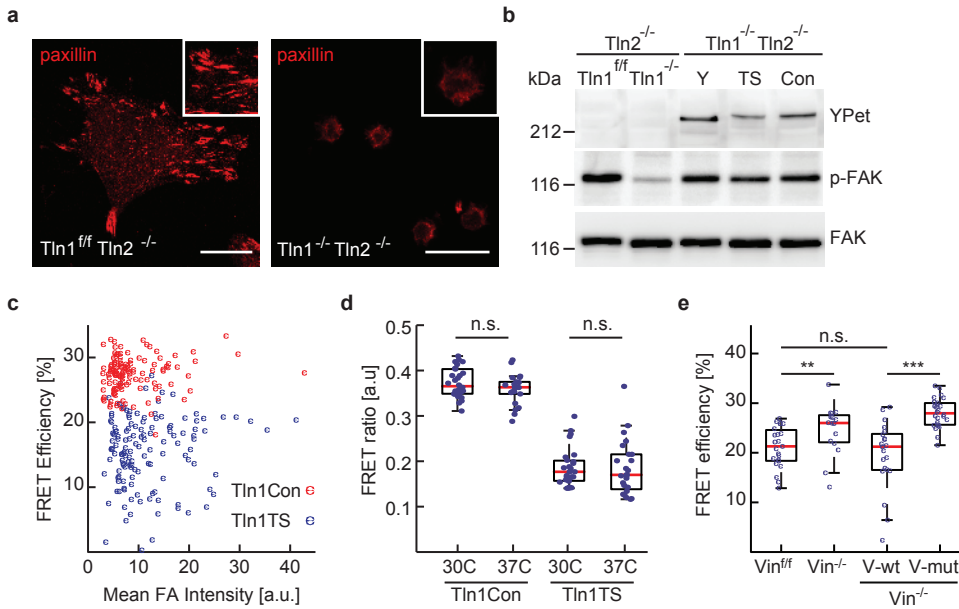
Computational codes. Mechanical fits were performed using previously published custom-written code^{24,42}; analysis software code runs on: IGOR Pro 6.31, 64-bit. Software for FA FRAP and TCSPC-FLIM analyses was generated specifically for the project and can be used in MATLAB. The data analysis algorithm for ratiometric FRET analyses is based on a previously published Focal Adhesion Tracking algorithm⁵⁴. All software is available on request.

41. Cecconi, C., Shank, E. A., Dahlquist, F. W., Marqusee, S. & Bustamante, C. Protein-DNA chimeras for single molecule mechanical folding studies with the optical tweezers. *Eur. Biophys. J.* **37**, 729–738 (2008).
42. Stigler, J., Ziegler, F., Gieseke, A., Gebhardt, J. C. & Rief, M. The complex folding network of single calmodulin molecules. *Science* **334**, 512–516 (2011).
43. von Hansen, Y., Mehlich, A., Pelz, B., Rief, M. & Netz, R. R. Auto- and cross-power spectral analysis of dual trap optical tweezer experiments using Bayesian inference. *Rev. Sci. Instrum.* **83**, 095116 (2012).
44. Mehlich, A., Austen, K., Ringer, P., Rief, M. & Grashoff, C. Evaluation of molecular tension sensors using single-molecule force spectroscopy and live cell FRET imaging. *Protoc. Exch.* <http://dx.doi.org/10.1038/protex.2015.095> (2015).
45. Subauste, M. C. et al. Rho family proteins modulate rapid apoptosis induced by cytotoxic T lymphocytes and Fas. *J. Biol. Chem.* **275**, 9725–9733 (2000).
46. Conti, F. J., Monkley, S. J., Wood, M. R., Critchley, D. R. & Muller, U. Talin 1 and 2 are required for myoblast fusion, sarcomere assembly and the maintenance of myotendinous junctions. *Development* **136**, 3597–3606 (2009).
47. Monkley, S. J. et al. Disruption of the talin gene arrests mouse development at the gastrulation stage. *Dev. Dyn.* **219**, 560–574 (2000).
48. Schiller, H. B. et al. β_1 - and $\alpha\text{-}$ class integrins cooperate to regulate myosin II during rigidity sensing of fibronectin-based microenvironments. *Nat. Cell Biol.* **15**, 625–636 (2013).
49. Sprague, B. L. & McNally, J. G. FRAP analysis of binding: proper and fitting. *Trends Cell Biol.* **15**, 84–91 (2005).
50. Carisey, A., Stroud, M., Tsang, R. & Ballestrem, C. Fluorescence recovery after photobleaching. *Methods Mol. Biol.* **769**, 387–402 (2011).
51. Goult, B. T. et al. The structure of an interdomain complex that regulates talin activity. *J. Biol. Chem.* **284**, 15097–15106 (2009).
52. Goksoy, E. et al. Structural basis for the autoinhibition of talin in regulating integrin activation. *Mol. Cell* **31**, 124–133 (2008).
53. Goult, B. T. et al. Structural studies on full-length talin1 reveal a compact auto-inhibited dimer: implications for talin activation. *J. Struct. Biol.* **184**, 21–32 (2013).
54. Wurflinger, T., Gamper, I., Aach, T. & Sechi, A. S. Automated segmentation and tracking for large-scale analysis of focal adhesion dynamics. *J. Microsc.* **241**, 37–53 (2011).
55. Yeung, T. et al. Effects of substrate stiffness on cell morphology, cytoskeletal structure, and adhesion. *Cell Motil. Cytoskeleton* **60**, 24–34 (2005).
56. Boudou, T., Ohayon, J., Picart, C., Pettigrew, R. I. & Tracqui, P. Nonlinear elastic properties of polyacrylamide gels: implications for quantification of cellular forces. *Biorheology* **46**, 191–205 (2009).
57. Lemonge, J., Sabass, B., Sun, B., Rogers, M. E. & Stone, H. A. Mechanics regulates ATP-stimulated collective calcium response in fibroblast cells. *J. R. Soc. Interface* **12**, 20150140 (2015).
58. Sabass, B., Gardel, M. L., Waterman, C. M. & Schwarz, U. S. High resolution traction force microscopy based on experimental and computational advances. *Biophys. J.* **94**, 207–220 (2008).
59. Jares-Erijman, E. A. & Jovin, T. M. FRET imaging. *Nat. Biotechnol.* **21**, 1387–1395 (2003).



Supplementary Figure 1 Single-molecule calibration of HP35-TS and HP35st-TS. (a) Filtered force-extension traces (FE) of consecutive stretch (blue) and relax (gray) cycles of HP35-TS; black solid lines are WLC model fits to the data marking folded and unfolded protein states. (b) FE of consecutive stretch (red) and relax (gray) cycles of HP35st-TS; black solid lines are WLC model fits to the data. (c) Superimposed HP35-TS (blue) and HP35st-TS (red) stretch and relax cycles; solid lines are entire data fits, dashed lines show WLC model fits. (d) Standard deviation of bead deflection fluctuations as a function of mean force for DNA-HP35-TS (blue), DNA-HP35st-TS (red) and only DNA (black). (e) Folding free energy distributions of HP35-TS (blue) and HP35st-TS (red); solid lines are Gaussian fits to the data. (f) Modelled force-extension curve using a two-state model with mechanical parameters of HP35st-TS. The dashed black line represents the folded state with zero contour length; the black solid line represents the completely unfolded state with contour length ; the red line indicates the average protein extension

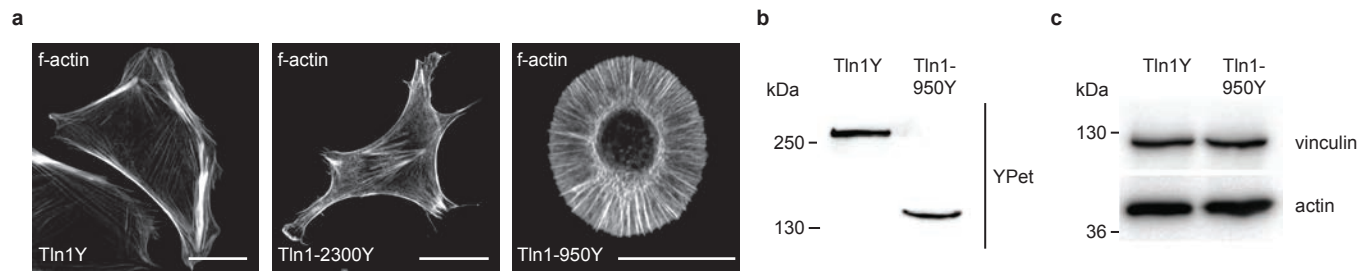
The corresponding probability plot for the folded and unfolded state is shown next to the force-extension plot. (g) Force-extension model fit for HP35st-TS using a three-state model (also shown in Fig. 1g, h). The dashed black line represents the folded state, the gray dashed line the half folded/unfolded state with contour length and the black solid line the completely unfolded state with contour length ; the red line indicates the average protein extension. The corresponding probability plot for the folded, half folded/unfolded and unfolded state is shown next to the force-extension plot. (h) Comparison of a two-state model fit with a three-state model fit to HP35-TS force-extension data (same data as in Fig. 1d). The residual plot in the upper graph indicates a better fit when a three-state model is used. (i) Protein stability curve for HP35 (black line) resulting from a combined fit to published experimental data. Data covering 0–40 °C (indicated as black empty squares) were taken from¹, data for 55–80 °C (indicated by the thick gray line) were derived from². Red circles mark the free energy values at 30 °C and 37 °C.



Supplementary Figure 2 The talin tension sensor rescues the talin-1 knockout phenotype. **(a)** Representative images from 3 independent experiments showing paxillin-stained (red) Tln1^{ff}/Tln2^{-/-} and Tln1^{-/-}/Tln2^{-/-} cells; note the lack of FA formation and cell spreading; scale bars, 20 μ m. **(b)** Representative western blots from 3 independent experiments demonstrating comparable expression levels and rescue of FAK phosphorylation in Tln1^{-/-}/Tln2^{-/-} cells by expression of Tln1Y (Y), Tln1TS (TS) and Tln1Con (Con); phospho-FAK blots indicate FAK pY-397. Unprocessed original scans of western blots are shown in Supplementary Fig. 5. **(c)** Live cell FRET efficiencies as a function of mean fluorescence intensities for Tln1TS (blue) and Tln1Con (red) ($n=129$ and 137 cells respectively; pooled from 5 independent experiments) indicating FRET efficiencies are

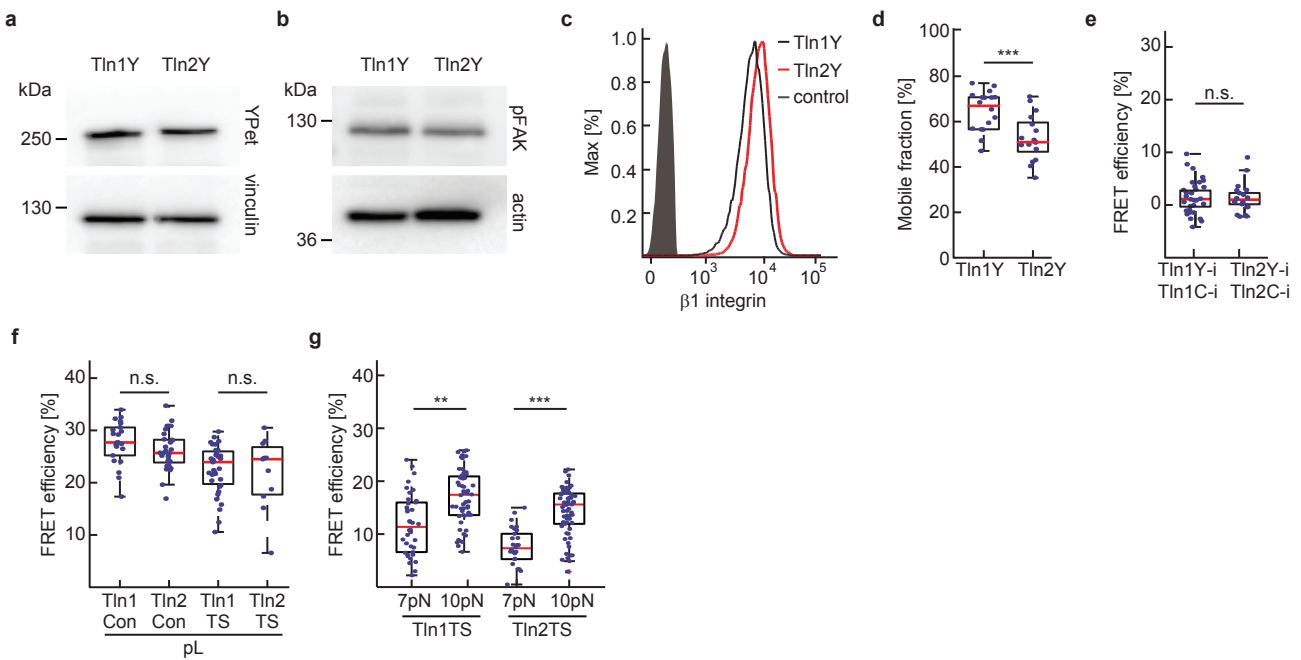
independent of the used fluorescence intensities. **(d)** Ratiometric FRET analysis of Tln1Con and Tln1TS cells imaged at 30 °C and 37 °C ($n=29$, 22 , 27 and 24 cells respectively from left to right; 3 independent experiments). **(e)** FRET increase in Tln1TS cells in the absence of vinculin indicates reduced tension across talin-1; re-expression of full length vinculin (V-wt), but not a mutant vinculin unable to engage the f-actin cytoskeleton (V-mut), rescues talin tension ($n=23$, 16 , 21 and 26 cells respectively from left to right; 3 independent experiments). **(d, e):** Kolmogorov-Smirnov test, ***: $p<0.001$; **: $p<0.01$; *: $p<0.05$; not significant (n.s.): $p > 0.05$. Boxplots indicate the median (red line) as well as 25th and 75th percentiles; whiskers reach out to 2.7 standard deviations (σ). Statistic source data are available in Supplementary Table 1.

SUPPLEMENTARY INFORMATION



Supplementary Figure 3 Effects of talin deletion mutants on the organization of the actin cytoskeleton. **(a)** Actin networks of the representative Tln1Y, Tln1-2300Y and Tln1950Y cells shown in Fig. 4b; note the lack of actin stress fibers in Tln1950Y cells; scale bars, 20 μ m.

(b, c) Representative western blots from 3 independent experiments demonstrating comparable talin **(b)** and vinculin **(c)** expression levels in Tln1Y and Tln1-950Y cells. Unprocessed original scans of western blots are shown in Supplementary Fig. 5.

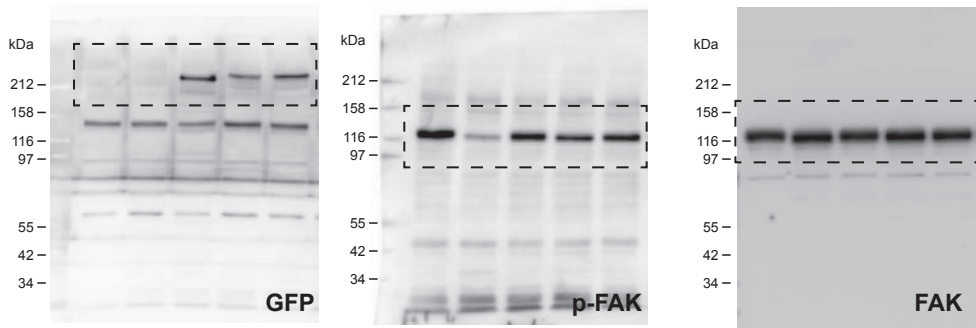


Supplementary Figure 4 Talin isoform studies. (a, b) Western blot analysis (3 independent experiments) of protein lysates from Tln1Y and Tln2Y cells demonstrating comparable expression levels and equal rescue of FAK phosphorylation. Unprocessed original scans of western blots are shown in Supplementary Fig. 5. (c) Representative FACS histogram of cells expressing Tln1Y (black) or Tln2Y (red) labelled for beta1 integrin; the negative control is shown in gray (4 independent experiments). (d) Reduced mobile fraction in Tln2Y expressing cells ($n=18$ (Tln1Y) and 17 (Tln2Y) cells; pooled from 3 independent experiments). (e) Intermolecular FRET analysis in cells co-expressing Tln1C-i/Tln1Y-i or Tln2C-i/Tln2Y-i seeded on FN-coated glass coverslips; note equally low intermolecular FRET levels ($n=31$ (Tln1C-i/Tln1Y-i) and 18 (Tln2C-i/Tln2Y-i) cells; 3 independent experiments). (f)

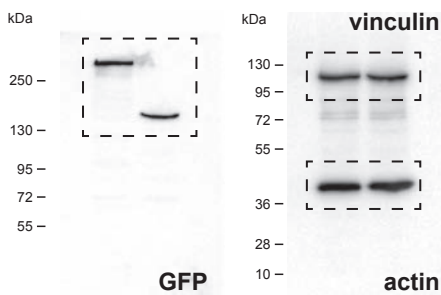
No FRET efficiency differences between Tln1Con and Tln2Con as well as Tln1TS and Tln2TS cells when seeded on pL-coated glass slides indicating integrin-specificity of isoform-specific differences ($n=22, 29, 35$ and 11 cells respectively from left to right; 3 independent experiments). (g) Elevated FRET efficiencies for HP35st (10 pN) probes in Tln1TS and Tln2TS as compared to HP35 (7 pN) when cells were seeded on FN-coated glass coverslips ($n=18, 27, 19$ and 27 cells respectively from left to right; 6 independent experiments). These data indicate that talin-2, similar to talin-1, is exposed to a range of forces. (d-g) Kolmogorov-Smirnov test. ***: $p<0.001$; **: $p<0.01$, not significant (n.s.): $p>0.05$. Boxplots indicate the median (red line) as well as 25th and 75th percentiles; whiskers reach out to 2.7 standard deviations (σ). Statistic source data are available in Supplementary Table 1.

SUPPLEMENTARY INFORMATION

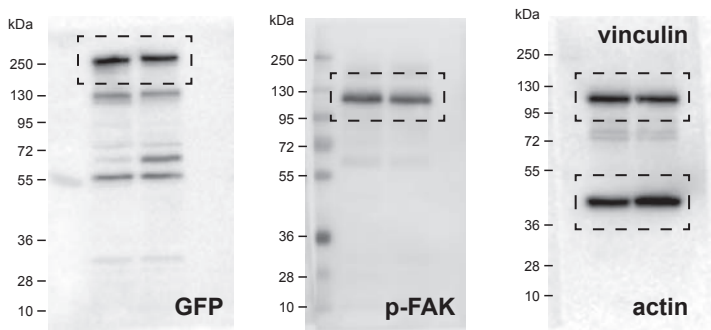
Supplementary Fig. 2b



Supplementary Fig. 3b, c



Supplementary Fig. 4a, b



Supplementary Figure 5 Unprocessed representative western blots. Black boxes with dashed lines indicate how blots were cropped for Supplementary Figs. 2, 3 and 4.

Supplementary Note: Single-molecule calibration of HP35-based tension sensors

Calibration data analysis. Within a certain regime optical traps can be treated as Hookean (linear-response) springs. To calculate forces, the beads' deflection out of the respective trap centre (x_{B1} and x_{B2}) can be multiplied by the trap stiffness (k_1 and k_2). The extension of the trap construct x_{tether} was assigned by subtracting the beads' deflection and the two bead diameters $2R$ from the distance d between the trap centres: $x_{tether} = d - 2R - x_{B1} - x_{B2}$. To improve the signal-to-noise ratio, the analysis was performed on the differential signal of the two beads³. From measured force-extension traces, we extracted mechanical parameters of the dsDNA handles as well as smHP35-TS using models for polymer elasticity. An extensible worm-like chain model (eWCL)⁴ was used to describe the mechanical response of the DNA where the force F_{eWLC} at extension x_D is given by eq. 1.

$$F_{eWLC}(x_D, [L_D, p_D, K]) = \frac{k_B T}{p_D} \left[\frac{1}{4\left(1 - \frac{x_D}{L_D} + \frac{F}{K}\right)^2} - \frac{1}{4} + \frac{x_D}{L_D} - \frac{F}{K} \right] \quad (\text{eq. 1})$$

Here, p_D is the persistence length, L_D the contour length and K the stretch modulus of the fitted DNA molecule. In our measurements, the value for the persistence length was approximately 22.5 nm and the stretch moduli were 300–400 pN; the temperature T was 303 K. With an average of 363 nm, our contour length corresponds reasonably well to the expected contour length of the two dsDNA handles (370 nm).

To model the behaviour of smHP35-TS under forces above the equilibrium transition when a well-defined length of totally unfolded protein is contributing to the overall force extension trace, we used a basic worm-like chain model (WLC)⁵ where F_{WLC} at protein extension x_P is given by eq. 2.

$$F_{WLC}(x_P, [L_P, p_P]) = \frac{k_B T}{p_P} \left[\frac{1}{4\left(1 - \frac{x_P}{L_P}\right)^2} - \frac{1}{4} + \frac{x_P}{L_P} \right] \quad (\text{eq. 2})$$

Here, p_P is the persistence length of unfolded protein and L_P its contour length; in our experiments we assumed p_P to be 0.7 nm. Eq. 1 and eq. 2 together allow fitting of the force-extension behaviour of the trap construct at forces above the unfolding transition by using the total contour length $L_{P,tot}$ of the fully unfolded protein as L_P in eq. 2. Within the time resolution of our experiments, we can assume the dsDNA handles to be at equilibrium with the unfolded protein such that the acting forces are equal: $F_{eWLC} = F_{WLC} = F$. Hence, the measured overall extension of the tether is given by eq. 3.

$$x_{tether}(F) = x_D(F) + x_P(F) \cdot p_{unf}(F) \quad (\text{eq. 3})$$

With $x_D(F)$ and $x_P(F)$ being the inverse of eq. 1 and eq. 2, and $x_P(F)$ containing contributions of the unfolded polypeptide chain weighted with the respective force-dependent probability $p_{unf}(F)$. Inversion of eq. 3 yields the force-extension relation of the entire tether.

Fitting force-extension data. To obtain an expression that can be used to fit the measured force-extension relation, a previous study presented a force-(trap)distance relation under equilibrium conditions for a protein consisting of N independent subunits each of which cooperatively unfolds and refolds⁶. Here, we commence a short derivation with the demand for the force F at the trap distance d being equal to the effective spring constant $k_{eff} = \left(\frac{1}{k_1} + \frac{1}{k_2}\right)^{-1}$ times the measured mean (or first moment) $\langle x \rangle$ of the sum of the measured deflections of both traps $x = x_{B1} + x_{B2}$

$$F(d) = k_{eff} \cdot \langle x \rangle \quad (\text{eq. 4})$$

With $p(x)$ being the distribution of x , we can express the first moment using equation 5.

$$\langle x \rangle = \int_{-\infty}^{+\infty} dx x \cdot p(x) \quad (\text{eq. 5})$$

With $H(x)$ being the energy function describing the entire system and the deflection x being a continuum of possible states, $p(x)$ can be written down as a Boltzmann distribution such as:

$$p(x) = \frac{1}{Z} \exp\left(-\frac{H(x)}{k_B T}\right) \quad (\text{eq. 6})$$

Here, $Z = \int_{-\infty}^{+\infty} dx \exp\left(-\frac{H(x)}{k_B T}\right)$ is the canonical partition function. Given that there are N subunits independently contributing to a measured mean deflection x , we present the energy function or Hamiltonian $H(x, i)$ of each of the $N+1$ possibly populated states including the assumption of equally sized subunits of same fractional energy in equation 7.

$$H(x, i) = \left(1 - \frac{i}{N}\right) \cdot \Delta G + \frac{1}{2} k_{eff} x^2 + \int_0^{d-x} F_{tether} \left(L_P = \frac{i}{N} \cdot L_{P,tot}, x_{tether}\right) dx_{tether} \quad (\text{eq. 7})$$

Where $i \in \{0, 1, 2, \dots, N\}$ and F_{tether} is the inverse of eq. 3 with $p_{unf}(F) = 1$. The first summand on the right hand side of eq. 7 contains the energy contribution of folded protein, the second summand comprises the two traps' stretching energy and the third summand the energy of the entire stretched tether consisting of dsDNA handles and unfolded protein. By setting

$\exp\left(-\frac{H(x)}{k_B T}\right) = \sum_{i=0}^N \exp\left(-\frac{H(x,i)}{k_B T}\right)$ in eq. 6, i.e. summing up all states' energy contributions, and using eq. 5, we obtain a general expression for a force-distance relation under equilibrium conditions from eq. 4 as presented in eq. 8.

$$F(d) = \frac{k_{eff}}{\int_{-\infty}^{+\infty} dx \sum_{i=0}^N \exp\left(-\frac{H(x,i)}{k_B T}\right)} \cdot \int_{-\infty}^{+\infty} dx x \cdot \sum_{i=0}^N \exp\left(-\frac{H(x,i)}{k_B T}\right) \quad (\text{eq. 8})$$

In case of a two- or a three-state equilibrium transition, N equals 1 or 2. A two-state transition is an ultrafast transition of a single cooperative unit switching between folded and unfolded state showing zero and full unfolded contour length $L_{P,tot}$ (Supplementary Fig. 1f). A three-state transition is composed of an additional cooperative unit, i.e. two cooperative units that unfold and fold independently from each other and thus can switch between three states in contour space: a completely folded or unfolded state as in the two-state transition and a ‘half’ folded/unfolded state, where one of the subunits is unfolded while the other one is folded (Supplementary Fig. 1g). For $N = 2$ the sum in the enumerator of eq. 8 is explicitly written down in eq. 9.

$$\begin{aligned} \sum_{i=0}^2 \exp\left(-\frac{H(x,i)}{k_B T}\right) = \\ \exp\left(-\frac{\Delta G + \frac{1}{2}k_{eff}x^2 + \int_0^{d-x} F_{tether}(L_P=0, x_{tether}) dx_{tether}}{k_B T}\right) + \\ \exp\left(-\frac{\frac{1}{2}\Delta G + \frac{1}{2}k_{eff}x^2 + \int_0^{d-x} F_{tether}(L_P=\frac{1}{2}L_{P,tot}, x_{tether}) dx_{tether}}{k_B T}\right) + \\ \exp\left(-\frac{\frac{1}{2}k_{eff}x^2 + \int_0^{d-x} F_{tether}(L_P=L_{P,tot}, x_{tether}) dx_{tether}}{k_B T}\right) \end{aligned} \quad (\text{eq. 9})$$

Using eq. 8, the free energy ΔG of the equilibrium transition can be calculated from fitting our measured force-distance relations. Importantly, our experiments are in good agreement with previous measurements where HP35 had been integrated between two ubiquitin domains⁶. The free energies equal $5.6 \pm 1 k_B T$ and $10.4 \pm 1 k_B T$ for HP35 ($n=338$) and HP35st ($n=344$) with forces at the equilibrium transition midpoint being 7.4 ± 0.5 pN and 10.6 ± 0.4 pN (Supplementary Fig. 1c, e and Fig. 1d).

In contrast to previous work⁶, however, HP35 dynamics were fitted best using a three-state instead of a two-state model. The better quality of the fit can be appreciated in Supplementary Fig. 1h. The deviation may be attributed to differences in peptide linkers that were used to construct the individual samples. HP35 was inserted between donor and acceptor fluorophore in HP35-TS using a very short

linker sequence (GS) to ensure efficient energy transfer, while it had been connected to ubiquitin domains by longer linker peptides before (ELGSSGG and GGSSGGT)⁶.

HP35-TS and HP35st-TS force–FRET relation. Due to our limited time resolution and the dragged motion of the trapped beads, we can only observe a mean deflection $\langle x \rangle$ during an equilibrium transition that can be converted into a mean protein extension $\langle x_p \rangle$. In case of either a two-state or three-state transition this mean value is the superposition of two or three fast interchanging states of distinct protein extension and thus FRET efficiencies. A relation between acting force F and observed FRET efficiency E_{FRET} in case of a two-state model is given in eq. 10.

$$E_{FRET}(F) = E_{FRET}(\langle x_p(F) \rangle) = E_{FRET}(x_f^0(F)) \cdot p_f(F) + E_{FRET}(x_u^{L_{tot}}(F)) \cdot p_u(F) \quad (\text{eq. 10})$$

Here, the mean extension is composed of the weighted contributions of two possible states, i.e. the folded state x_f^0 with zero contour length and the unfolded state $x_u^{L_{tot}}$ with full contour length L_{tot} . The subscript indicates the state and the superscript the corresponding contour length. The probability $p_u(F)$ to be unfolded can be directly read off the force-extension plot by building the ratio between the mean extension given by the fit and the full extension (Supplementary Fig. 1f). As the sum of folding and unfolding probabilities has to equal one, we can conclude: $p_f(F) = 1 - p_u(F)$. Expanding eq. 10 towards the three-state model with two independently folding and unfolding subunits of half the entire protein's contour length and each comprising half of the overall free energy leads us to eq. 11.

$$E_{FRET}(F) = E_{FRET}(x_f^0(F)) \cdot p_f^{3s}(F) + E_{FRET}(x_h^{L_{tot}/2}(F)) \cdot p_h^{3s}(F) + E_{FRET}(x_u^{L_{tot}}(F)) \cdot p_u^{3s}(F) \quad (\text{eq. 11})$$

Here the additional half folded/unfolded state $x_h^{L_{tot}/2}$ shows up when one of the subunits is folded while the other one is unfolded. The probabilities for the three states cannot be directly read off from the corresponding force-extension plot, but they can be derived from the folding and unfolding probabilities of the two subunits $j \in \{1,2\}$, namely $p_{j,f}(F)$ and $p_{j,u}(F)$. The folded state is observed when both subunits are folded at the same time, for this the probability is $p_f^{3s}(F) = p_{1,f}(F) \cdot p_{2,f}(F)$; the same argument leads us to $p_u^{3s}(F) = p_{1,u}(F) \cdot p_{2,u}(F)$. The half folded/unfolded state has two possible configurations leading to the observable contour length $L_{tot}/2$ and can be expressed like this: $p_h^{3s}(F) = p_{1,f}(F) \cdot p_{2,u}(F) + p_{1,u}(F) \cdot p_{2,f}(F)$. As the subunits have identical probabilities, we can rewrite eq. 11 using only the two-state probabilities of the subunits as presented in the shortened form of eq. 12.

$$E_{FRET}(F) = E_{FRET}\left(x_f^0(F)\right) \cdot \left\{ [p_{j,f}(F)]^2 \right\} + E_{FRET}\left(x_h^{L_{tot}/2}(F)\right) \cdot \left\{ 2 \cdot p_{j,f}(F) \cdot p_{j,u}(F) \right\} + \\ E_{FRET}\left(x_u^{L_{tot}}(F)\right) \cdot \left\{ [p_{j,u}(F)]^2 \right\} \quad (\text{eq. 12})$$

Considering the experimentally observed zero-force FRET efficiency of 30 % and a Förster radius of 5.8 nm, we assumed the inter-chromophore separation to be 6.7 nm in the absence of force and thus for the entirely folded state. Note that $x_f^0(F)$ is actually not force-dependent as zero contour length cannot be stretched beyond zero yielding $E_{FRET}\left(x_f^0(F)\right) = 0.3$ at any times. The other states' contributions to the FRET efficiency are deduced by adding their force-dependent extensions to the intrinsic 6.7 nm fluorophore separation.

Temperature dependence of the calibration. The single-molecule calibration measurements were performed at room temperature. Due to the used laser intensity of about 1.2 W, we can estimate the temperature at the position of the protein under study to be approximately 30 °C according to previous publication⁷. As experiments with cells were conducted at 37 °C the corresponding temperature-dependent change of the free energy needs to be accounted for, especially as this implies a change of the sensors' force sensitivity as well. The plot of the free energy of unfolding as a function of temperature is called stability curve⁸. To estimate the maximal expected relative deviation of ΔG between 30 °C and 37 °C, we derived a stability curve for HP35 from published data^{1, 2}. The model used for fitting as in² is given by equations 13 to 15.

$$\Delta G = \Delta H(T) - T\Delta S(T) \quad (\text{eq. 13})$$

$$\Delta H = \Delta H(T_{trs}) + \Delta c_{p,T_{trs}}(T - T_{trs}) + \frac{1}{2}\alpha(T - T_{trs})^2 \quad (\text{eq. 14})$$

$$\Delta S = \frac{\Delta H(T_{trs})}{T_{trs}} + (\Delta c_{p,T_{trs}} - \alpha T_{trs}) \ln\left(\frac{T}{T_{trs}}\right) + \alpha(T - T_{trs}) \quad (\text{eq. 15})$$

While fitting the data points in the lower temperature range from 0–40 °C and considering their respective errors, the fitting parameters were constrained such that the curve shape at high temperatures was recovered as well (Supplementary Fig. 1i). The starting values were chosen according to²: $T_{trs} = 337$ K, $\Delta H(T_{trs}) = 118$ kJ/mol, $\Delta c_{p,T_{trs}} = 2.66$ kJ/mol, $\alpha = -0.0247$ kJ/mol. Reading off the ΔG values from the resulting stability curve at 30 °C and 37 °C yields an absolute change in energy of ± 1.3 kJ/mol, i.e. $\sim 0.5 k_B T$ with respect to the calibration at 30 °C. The relative deviation is a drop in energy by 15 %. The deduced impact on the force sensitivity maximum is a drop

of up to 0.6 pN for HP35 and 1.0 pN for HP35st, i.e. about 10 %. Importantly, even though the regions of highest sensor sensitivity slightly shift, they are always well separated.

References

1. Buscaglia, M., Kubelka, J., Eaton, W.A. & Hofrichter, J. Determination of ultrafast protein folding rates from loop formation dynamics. *J. Mol. Biol.* **347**, 657-664 (2005).
2. Godoy-Ruiz, R. *et al.* Estimating free-energy barrier heights for an ultrafast folding protein from calorimetric and kinetic data. *J Phys Chem B* **112**, 5938-5949 (2008).
3. Moffitt, J.R., Chemla, Y.R., Izhaky, D. & Bustamante, C. Differential detection of dual traps improves the spatial resolution of optical tweezers. *Proceedings of the National Academy of Sciences of the United States of America* **103**, 9006-9011 (2006).
4. Wang, M.D., Yin, H., Landick, R., Gelles, J. & Block, S.M. Stretching DNA with optical tweezers. *Biophys. J.* **72**, 1335-1346 (1997).
5. Bustamante, C., Marko, J.F., Siggia, E.D. & Smith, S. Entropic elasticity of lambda-phage DNA. *Science* **265**, 1599-1600 (1994).
6. Zoldak, G., Stigler, J., Pelz, B., Li, H. & Rief, M. Ultrafast folding kinetics and cooperativity of villin headpiece in single-molecule force spectroscopy. *Proceedings of the National Academy of Sciences of the United States of America* **110**, 18156-18161 (2013).
7. Peterman, E.J., Gittes, F. & Schmidt, C.F. Laser-induced heating in optical traps. *Biophys. J.* **84**, 1308-1316 (2003).
8. Becktel, W.J. & Schellman, J.A. Protein stability curves. *Biopolymers* **26**, 1859-1877 (1987).